

# Regional PM<sub>2.5</sub> pollution confined by atmospheric internal boundaries in the North China Plain: boundary layer structures and numerical simulation

Xipeng Jin<sup>1</sup>, Xuhui Cai<sup>1\*</sup>, Mingyuan Yu<sup>2</sup>, Yu Song<sup>1</sup>, Xuesong Wang<sup>1</sup>, Hongsheng Zhang<sup>3</sup>, Tong Zhu<sup>1</sup>

<sup>1</sup>College of Environmental Sciences and Engineering, State Key Lab of Environmental Simulation and Pollution Control, Peking University, Beijing 100871, China

<sup>2</sup>School of Applied Meteorology, Nanjing University of Information Science and Technology, Nanjing 210044, China

<sup>3</sup>Department of Atmospheric and Oceanic Sciences, School of Physics, Peking University, Beijing 100871, China

*Correspondence to:* Xuhui Cai (E-mail: xhcai@pku.edu.cn)

1 **Abstract.** This study reveals mesoscale planetary boundary layer (PBL) structures under various  
2 pollution categories during autumn and winter in the North China Plain. The role of the atmospheric  
3 internal boundaries (AIBs, referring to the discontinuity of meteorological conditions in the lateral  
4 direction) in regulating PBL structure and shaping the PM<sub>2.5</sub> pollution patterns is emphasized. The  
5 Weather Research and Forecast model is used to display the three-dimensional meteorological fields, and  
6 its performance is evaluated by surface observations and intensive soundings. The evaluation  
7 demonstrates that the model reasonably captures the mesoscale processes and the corresponding PBL  
8 structures. Based on the reliable simulations, three typical pollution cases are analyzed. Case-1 and Case-  
9 2 represent the two main modes of the wind shear category pollution, which is featured with airflow  
10 convergence line/zone as AIB and thus is dominated by dynamical effect. Case-1 presents the west-  
11 southwest wind shear mode associated with a trough convergence belt. The convergent airflow layer is  
12 comparable to the vertical scale of the PBL, allowing PM<sub>2.5</sub> transport to form a high pollution area. Case-  
13 2 exhibits another mode with south-north wind shear. A "lying Y-shaped" convergence zone is formed  
14 with a thickness of about 3000m, extending beyond the PBL. It defines a clear edge between the southern  
15 polluted airmass and the clean air in the north. Case-3 represents the topographic obstruction category,  
16 which is characterized by a cold-air damming AIB in front of the mountains. The PBL at the foothills is  
17 thermally stable and dynamically stagnant due to the capping inversion and the convergent winds. It is  
18 in sharp contrast to the well-mixed/ventilated PBL in the southern plains, especially in the afternoon. At  
19 night, this meteorological discontinuity becomes less pronounced. The diurnal variation of the PBL  
20 thermal-dynamical structure causes the pollutants to concentrate at the foot of the mountains during the

21 daytime and locally accumulate throughout the entire plain in the evening. These results provide a more  
22 complete mesoscale view of the PBL structure and highlight its spatial heterogeneity, which promotes  
23 the understanding of air pollution at the regional scale.

24 **Keywords:** Boundary layer structure; atmospheric internal boundaries; PM<sub>2.5</sub>; modeling

## 25 **1 Introduction**

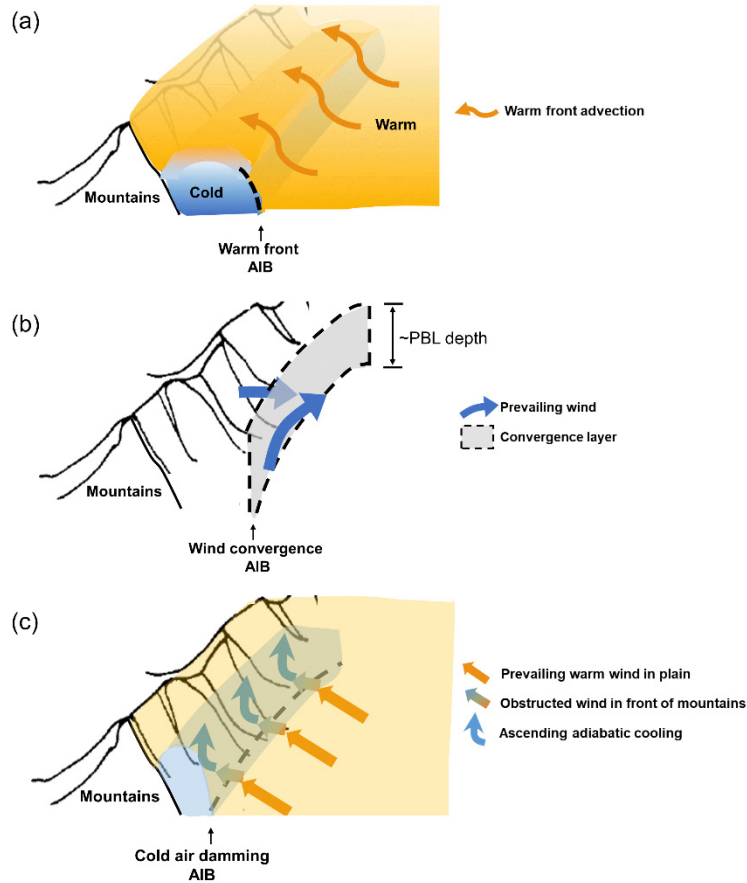
26 The planetary boundary layer (PBL) is the lowest section of the atmosphere that responds directly  
27 to the heat and friction from the Earth's surface (Stull, 1988; Garratt, 1992). Most air pollutants are  
28 intensively emitted or chemically produced within this layer, and their horizontal transport and vertical  
29 mixing are affected by the dynamical flow and thermal stability of the PBL (Tennekes, 1974). Therefore,  
30 the PBL structure plays a crucial role in the evolution, magnitude and distribution of air pollution.

31 The PBL structure has been recognized to be strongly dependent on three categories of factors: (i)  
32 the single-column vertical property (such as turbulence intensity) forced by the local surface's energy  
33 balance; (ii) the lateral-section horizontal variation of wind, temperature and humidity regulated by the  
34 mesoscale meteorological process and (iii) the three-dimensional spatial evolution controlled by the  
35 large-scale synoptic system (Boutle et al., 2010). The local vertical PBL structure and its impact on air  
36 pollution have been widely discussed from different aspects including turbulent mixing (Emeis and  
37 Schafer, 2006; Ren et al., 2019), dynamical effect (Dupont et al., 2016), entrainment (Li et al., 2018; Jin  
38 et al., 2020), and radiative feedback with aerosol (Petaja Petäjä et al., 2016). In these studies, the PBL  
39 height at a certain site has been the most commonly used indicator to analyze the correlation with  
40 pollutant concentration, whether from the time scale of the diurnal cycle, daily variation, or longer period  
41 (Bianco et al., 2011; Liu et al., 2019; Miao and Liu, 2019). Moreover, some studies investigate the PBL  
42 spatial structure under the large-scale force of weather systems (Prezerakos, 1998; Boutle et al., 2010;  
43 Mayfield and Fochesatto, 2013). Sinclair et al. (2010) report the three-dimensional PBL structure  
44 developed beneath an idealized mid-latitude weather system, which is characterized by a deep convective  
45 PBL in the eastern flanks of the anticyclone and a shallow shear-driven PBL in the cyclone's warm sector.  
46 The effect of the monsoon trough on the PBL has also been indicated, showing relatively low PBL capped  
47 by a stable layer in the western end of the trough line, while a well-defined deep moist layer with active  
48 thermal instability in the eastern end (Rajkumar et al., 1994; Narasimha, 1997; Potty et al., 2001). In  
49 recent years, synoptic classification has been used to explore the role of different weather circulations on  
50 PBL structure and to further analyze air pollution (Peng et al., 2016; Xiao et al., 2020). The movement  
51 of the synoptic systems makes the shallow and deep boundary layers develop alternately in a certain area,  
52 regulating the periodic evolution of large-scale air pollution.

53 As the intermediate scale, mesoscale systems interact with PBL in more direct and complex ways,

54 since they occur in the lower troposphere with vertical extension comparable with the PBL depth and  
55 horizontal scale close to the regional range. Discontinuity of meteorological properties inside and outside  
56 these systems presents as atmospheric internal boundaries (AIBs) in the lateral direction, usually  
57 manifested as temperature contrast and/or wind shift. Previous studies have emphasized their influence  
58 on the initiation of convective storms (Sanders and Doswell, 1995; Hane et al., 2002; Bluestein, 2008).  
59 On the other side, as internal lateral boundaries within the low-level atmosphere, the AIBs can lead to  
60 the abrupt change of the PBL spatial structure, which is of particular importance to the evolution of  
61 regional pollution. The effects of mesoscale sea-land and mountain-valley circulations on the PBL have  
62 been clarified, i.e., the thermal internal boundary layer in the coastal area and the depressed PBL close  
63 to a mountain base (Garratt, 1990; Lu and Turco, 1995; Talbot et al., 2007; De Wekker, 2008; Miao et  
64 al., 2015). Some studies discuss the PBL structure under the rule of other types of mesoscale/sub-synoptic  
65 scale systems, such as the persistent cold-air pools in the Salt Lake valley (Lareau et al., 2013), foehn  
66 winds in the Eastern Alps (Seibert, 1990; Baumann et al., 2001), and leeside troughs and cold-air  
67 damming around the Appalachian mountains (Seaman and Michelson, 2000; Bell and Bosart, 1988), as  
68 well as the frequent cold and warm fronts in Europe (Berger and Friche, 1995; Sinclair, 2013). However,  
69 there needs more understanding of their impact on the evolution of air pollution.

70 The North China Plain (NCP) is one of the most polluted areas in the world. The dense population  
71 and developed industries produce intensive emissions in this region, with most sources located in the  
72 plain area and less in the northern and western mountains (their spatial distribution is presented in ~~the~~  
73 ~~supplement material~~ Fig. S1). High-intensity primary emissions are the fundamental cause of air  
74 pollution, which directly releases pollutants into the atmosphere and provides precursors for secondary  
75 aerosol formation (Lyu et al., 2016; Zhao et al., 2019). In order to improve the air quality, a series of  
76 stringent emission reduction policies are implemented from 2013, which make the annual mean PM<sub>2.5</sub>  
77 concentrations decrease by 32% in 2017 (Zhang et al, 2019). However, the severe polluted days still  
78 occur frequently, especially in winter (Zhang et al., 2018). During these pollution episodes, adverse  
79 meteorological conditions are the dominant factors causing high pollution levels and various spatial  
80 patterns, as there are no significant changes in emissions in a short period (e.g., weeks). Extensive studies  
81 have been conducted to investigate the meteorological causes of regional pollution in the NCP, such as  
82 the local meteorological factors and large-scale synoptic process (Ye et al., 2016; Ren et al., 2019; Li et  
83 al., 2020). Nevertheless, the knowledge about the PBL spatial structures under the impact of the  
84 mesoscale AIBs is still insufficient, and the role of the special PBL structures plays in the air pollution  
85 evolution at a regional scale is even unclear (Bluestein, 2008; McNider and Pour-Biazar, 2020).



86  
 87 Figure 1. Schematic diagram showing the conceptual model of PBL spatial structures under three  
 88 pollution categories. (a) Frontal category: the blue-shaded and orange-filled areas represent the isolated  
 89 and stable cold air mass ahead of the warm front and the warmer well-mixing atmosphere behind the  
 90 front. The orange arrows indicate warm front advection. (b) Wind shear category: two blue arrows  
 91 represent the airflows ahead of and behind the trough. The gray-filled area indicates the dynamical  
 92 convergence layer with a depth comparable to the boundary layer height. (c) Topographic obstruction  
 93 category: the light blue filled area indicates the cold air damming at the foot of the windward mountains.  
 94 Terrain obstruction disrupts the geostrophic balance so that the southerly warm advection weakens (long  
 95 orange arrows) and turns to the easterly cold advection (short gradient-color arrows), and meanwhile, the  
 96 air mass accumulates to produce a lift cooling (up blue arrows). Black dashed lines in (a-c) indicate the  
 97 warm front AIB, wind convergence AIB, and cold air damming AIB respectively. The PBL spatial  
 98 structure under the first category has been revealed by Jin et al. (2021). For the latter two categories, their  
 99 PBL three-dimension structures are discussed in Sect 3.3 in this paper.

100 Based on the surface observations, a thorough survey of the PM<sub>2.5</sub> pollution categories under the  
 101 control of the AIBs is carried out by Jin et al. (2022, ~~submitted~~). It is found that the pollution formation-  
 102 maintenance process in the NCP can be classified into three categories, i.e., the frontal category, wind  
 103 shear category and topographic obstruction category during the autumn and winter of the investigated 7

104 years (2014–2020). Figure 1 shows the schematic diagram of three pollution categories corresponding to  
105 various AIBs. The frontal category represents about 41 % of all 98 pollution episodes, and its PBL spatial  
106 structure has been revealed in a previous case study (Jin et al., 2021). It is characterized by an isolated  
107 cold air mass, which is laterally confined by mountains and warm front AIB, and vertically covered by a  
108 warm dome (Fig. 1a). The strong elevated inversion depresses the PBL height abruptly to 200~300 m  
109 within the cold area in contrast to 600~800 m outside the zone, constituting adverse dispersion conditions  
110 and resulting in the most serious PM<sub>2.5</sub> pollution. The wind shear category is associated with airflow  
111 convergence AIB (Fig. 1b), which is dominated by dynamical effect and causes lighter PM<sub>2.5</sub> pollution.  
112 West-southwest wind shear and south-north wind shear are the two main modes. The third category  
113 occurs when the airflow cannot cross the topographic obstruction and form the cold air damming AIB. A  
114 cold and heavy pollution belt develops at the foot of the windward mountains (Fig. 1c), under the  
115 synergistic effect of dynamical obstruction and thermal stratification. Although previous studies have  
116 classified the air pollution and revealed the spatial characteristics of the first category, the three-  
117 dimensional PBL structures interacting with AIBs under the other two categories are not yet clarified,  
118 which is responsible for 43% of pollution episodes in the NCP. In order to fulfill this knowledge gap, the  
119 present study deeply analyzes representative cases of wind shear category and topographic obstruction  
120 category (Detailed analyses in Sect 3.3), and aims to provide a complete conceptual model of the PBL  
121 spatial structure in the NCP under various pollution categories and corresponding AIBs (Fig.1).

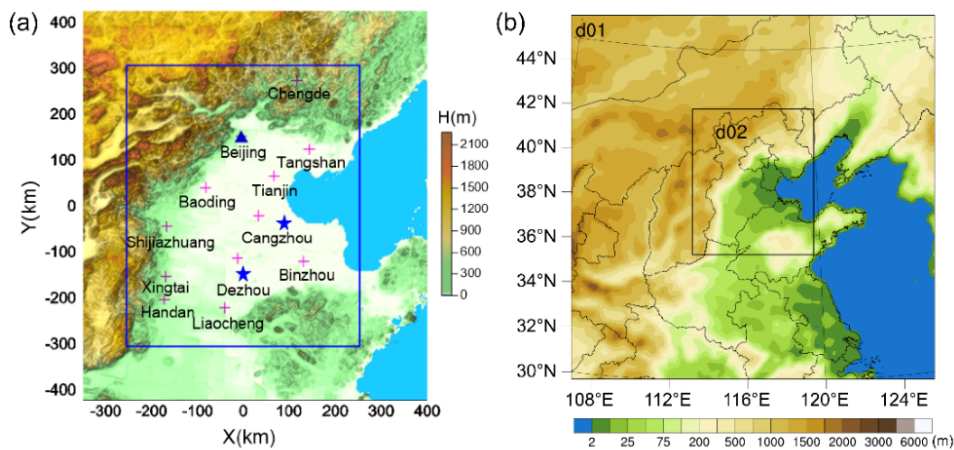
122 The mesoscale meteorological models, such as the Weather Research and Forecast (WRF) with the  
123 high spatial and temporal resolution, are plausible tools to capture the mesoscale systems and display  
124 detailed spatial structures in the lower atmosphere, including the AIBs and the PBL (Jimenez et al., 2016,  
125 Pielke and Uliasz, 1998; Seaman, 2000; Hanna and Yang, 2001; McNider and Pour-Biazar, 2020). The  
126 present study tries to reveal the thermal and dynamical structures of the PBL and their evolution  
127 associated with different AIBs in the condition of pollution episodes, by using the WRF model. For this  
128 purpose, the model performance is at first evaluated with detailed sounding data from intensive  
129 experiments, to ensure the model's ability in reproducing the meteorological fields and their three-  
130 dimensional structures in the concerned region. The article is organized as follows. The following section  
131 describes the PBL sounding observations as well as the WRF model settings. Section 3 provides an  
132 overview of representative pollution cases and the evaluation of the model performance. Furthermore,  
133 the PBL spatial structures under various pollution categories are analyzed. Finally, the conclusions are  
134 presented and the uncertainty of mesoscale numerical simulation is discussed in Sect. 4.

135 **2 Data and methods**

136 **2.1 Observations and data analysis**

137 **Intensive GPS (Global Positioning System) sounding data:** Two periods of field experiments  
138 were carried out to evaluate the meteorological model and explore wintertime PBL structure in the NCP:  
139 at Cangzhou (38°13' N, 117°48' E, Fig. 2a) from January 8 to 28, 2016 and at Dezhou (37°16' N, 116°43'  
140 E, Fig. 2a) from December 25, 2017, to January 24, 2018. GPS radiosonde (Beijing Changzhi Sci & Tech  
141 Co. Ltd., China) was used to obtain profiles of wind speed, wind direction, temperature, and relative  
142 humidity with a vertical resolution of approximately 1 s (3~5 m). Eight soundings were taken on each  
143 day, at 0200, 0500, 0800, 1100, 1400, 1700, 2000 and 2300 LT (i.e., Local Time = Universal Time  
144 Coordinated + 8). The reliability of the GPS sounding data has been systematically evaluated by Li et al.  
145 (2020) and Jin et al. (2020, 2021).

146 **Routine radiosonde sounding data:** Routine sounding data from the meteorological station of  
147 Beijing (39°56' N, 116°17' E, Fig. 2a) were collected during October 7–12, 2014, in the absence of  
148 intensive PBL observation. The data were obtained from Wyoming University, USA  
149 (<http://weather.uwyo.edu.html>), and the original observation data with higher vertical resolution were  
150 provided by the China Meteorological Administration. The routine soundings were taken 2 times a day,  
151 at 0800 and 2000 LT.



152  
153 Figure 2. Geographical map of the (a) observation area and (b) WRF model domain. Intensive GPS  
154 soundings at Dezhou and Cangzhou (star), routine radiosonde sounding at Beijing (triangle) and air  
155 quality stations (plus) are indicated in (a). The rectangle in (a) is the same as the model inner domain d02  
156 in (b).

157 **PBL height and vertical profiles:** During the two periods of intensive field experiments, 160 and  
158 240 datasets were collected at these two sites, including vertical profiles of temperature, relative humidity,  
159 wind speed, and wind direction. We carried out quality control on the original sounding data and

160 eliminated outliers and then calculated the profiles of potential temperature. All the profiles were  
161 smoothed by a three-point moving average method and were interpolated to obtain a vertical resolution  
162 of 10 m. The PBL height was derived via the potential temperature profile method and the detailed  
163 calculation followed the mathematical method established by Liu and Liang (2010). Sounding data were  
164 used to evaluate the model performance and to analyze the three-dimensional thermal and dynamical  
165 spatial structure of the PBL.

166 In addition to the PBL sounding data, routine meteorological observation and air quality monitoring  
167 data were used to obtain the surface meteorological field and pollutant concentration field. The spatial  
168 distributions of sea level pressure, 10 m wind vector, potential temperature, and the corresponding PM<sub>2.5</sub>  
169 concentration were obtained by data interpolation or diagnostic model, details of the methods were  
170 referred to Jin et al. (2021).

## 171 **2.2 WRF model simulations**

172 The WRF model was used to investigate the vertical and horizontal structures of the PBL. Two  
173 nested domains (Fig. 2b) were employed with horizontal grid resolutions of 15 and 5 km. Each domain  
174 had 37 vertical layers extending from the surface to 100 hPa, with 25 layers within 2 km (with the  
175 respective height of about 9 m, 25 m, 50 m, 85 m, 120 m, 160 m, 200 m, 240 m, 290 m, 350 m, 420 m,  
176 500 m, 580 m, 660 m, 740 m, 820 m, 900 m, 980 m, 1080 m, 1200 m, 1350 m, 1550 m, 1700m, 1850 m,  
177 and 2000 m) to resolve the PBL structure. The meteorological initial and boundary conditions were set  
178 using the United States National Center for Environmental Prediction Final Analysis (NCEP-FNL)  
179 dataset. The physics parameterization schemes applied in this study were the same as Jin et al. (2021).

## 180 **2.3 Representative cases**

181 As mentioned above, PM<sub>2.5</sub> pollution episodes in the NCP are identified in the frontal category, wind  
182 shear category, and topographic obstruction category, according to their association with the mesoscale  
183 AIBs (Jin et al., 2022 [submitted](#)). The present study tries to reveal the PBL structures modified by the  
184 AIBs under various pollution categories. Among them, the first category has been investigated previously  
185 (Jin et al., 2021). We focus on the representative cases under the other two categories in this paper. For  
186 the wind shear category, there are two main shear modes: west-southwest wind shear and south-north  
187 wind shear. Therefore a total of three typical cases are selected to respectively represent these two  
188 pollution categories, i.e., Case-1 for west-southwest wind shear mode: during January 17–21, 2018;  
189 Case-2 for south-north wind shear mode: during January 7–11, 2016; and Case-3 for topographic  
190 obstruction category: during October 7–12, 2014. The temporal and spatial evolution of their PM<sub>2.5</sub>  
191 concentrations and the corresponding surface meteorological conditions would be analyzed based on  
192 routine observations, and their PBL spatial structures would be revealed by the WRF model simulations.

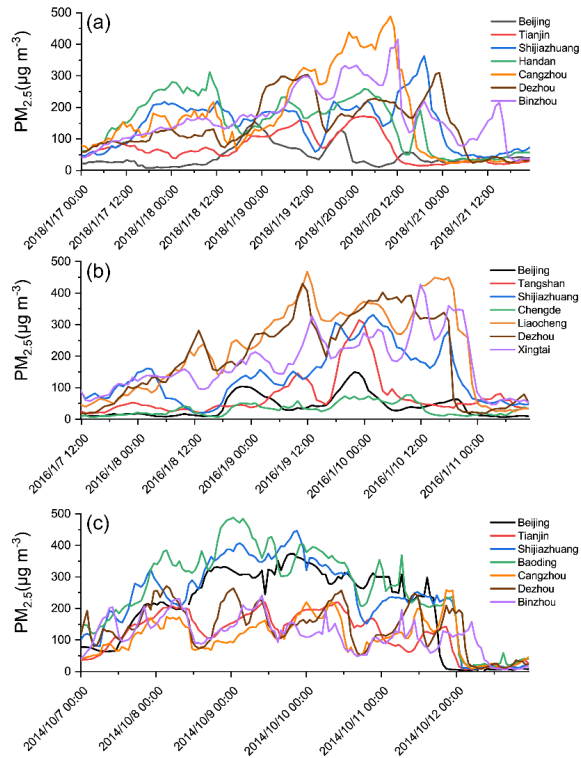
## 193 3 Results

### 194 3.1 Basic features of the cases

195 The surface observations for these three cases are presented firstly. According to the temporal  
196 evolution of  $PM_{2.5}$  concentration at different stations in the NCP (Fig. 3), all of these three pollution  
197 episodes went through the stages of formation, maintenance and diffusion. As shown in Fig. 3a, Case-1  
198 was characterized by two main concentration peaks ( $300 \mu g m^{-3}$  at Handan vs  $500 \mu g m^{-3}$  at Cangzhou)  
199 in the formation-maintenance stage (January 17–20, 2018), with the latter being higher than the former.  
200 From noon on January 20, 2018, pollution in Tianjin-Cangzhou-Shijiazhuang diffused successively and  
201 all sites reached a clean level on the afternoon of January 21, 2018. For Case-2, the pollution formed in  
202 the first two days, maintained over the next day and was cleaned on the night of January 10, 2016 (Fig.  
203 3b). The southern sites such as Liaocheng and Dezhou were the most polluted (reaching  $450 \mu g m^{-3}$ ) and  
204 the northern cities such as Beijing and Chengde were the least polluted (less than  $150 \mu g m^{-3}$ ). Pollution  
205 in Case-3 experienced the formation process on October 7–8, 2014, maintained for the successive three  
206 days, and ended on October 12, 2014 (Fig. 3c). During this period, the piedmont sites (Baoding, Beijing  
207 and Shijiazhuang) kept always a high concentration regardless of day and night (about  $400 \mu g m^{-3}$ ), while  
208 the southeast sites (Binzhou, Dezhou and Cangzhou) had lighter pollution and obvious diurnal cycle  
209 (lower than  $250 \mu g m^{-3}$ ).

210 The spatial patterns of  $PM_{2.5}$  pollution, from the formation (Fig. 4i), maintenance (Fig. 4ii-iv), to  
211 the diffusion stage (Fig. 4v), are illustrated for each case. In the formation stage, the polluted air mass of  
212 Case-1 and Case-3 built up along the mountains from the southwest of the NCP, with the latter being  
213 more concentrated and the former being widespread in the south (Fig. 4a-i, c-i). While the pollution in  
214 Case-2 first developed from the south (Fig. 4b-i). During the pollution maintenance process, Case-1 was  
215 featured with extensive  $PM_{2.5}$  flooding the NCP, making the eastern region gradually covered by heavy  
216 pollution (Fig. 4a, ii-iv); in Case-2, a polluted air mass has been advancing northward with a clear edge,  
217 but it did not reach the northern mountainous area (Fig. 4b, ii-iv); the spatial distribution of  $PM_{2.5}$  of  
218 Case-3 was characterized by the day-night contrast, manifested as pollution filling the entire plain area  
219 at night while concentrating in front of the mountains with a distinct edge on the southeast side during  
220 the daytime (Fig. 4c, ii-iv). Finally, these pollution cases were diffused in different ways. In Case-1, the  
221 clean air first occupied the northern parts of the NCP with a large concentration gradient on the front  
222 edges (Fig. 4a, v). As for Case-2,  $PM_{2.5}$  was restored to a clean level from the northeast (Fig. 4b, v).  
223 Pollution in the northwest was earliest removed in Case-3, with Beijing acting like a  
224 loophole/passageway in the cleaning process (Fig. 4c, v). These cases presented various pollution  
225 distributions, however, all of them were characterized by clear edges or distinct heavy pollution cores.

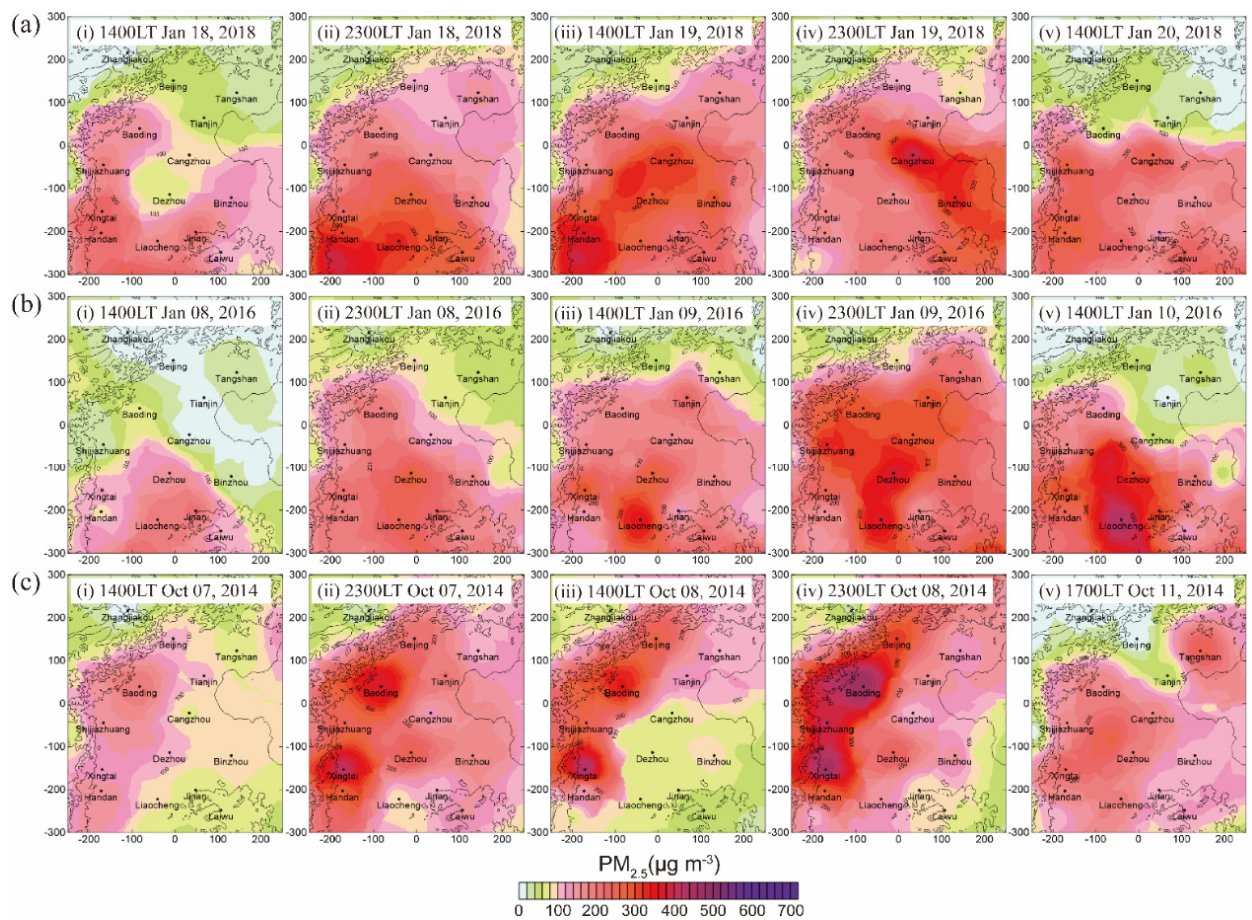




226

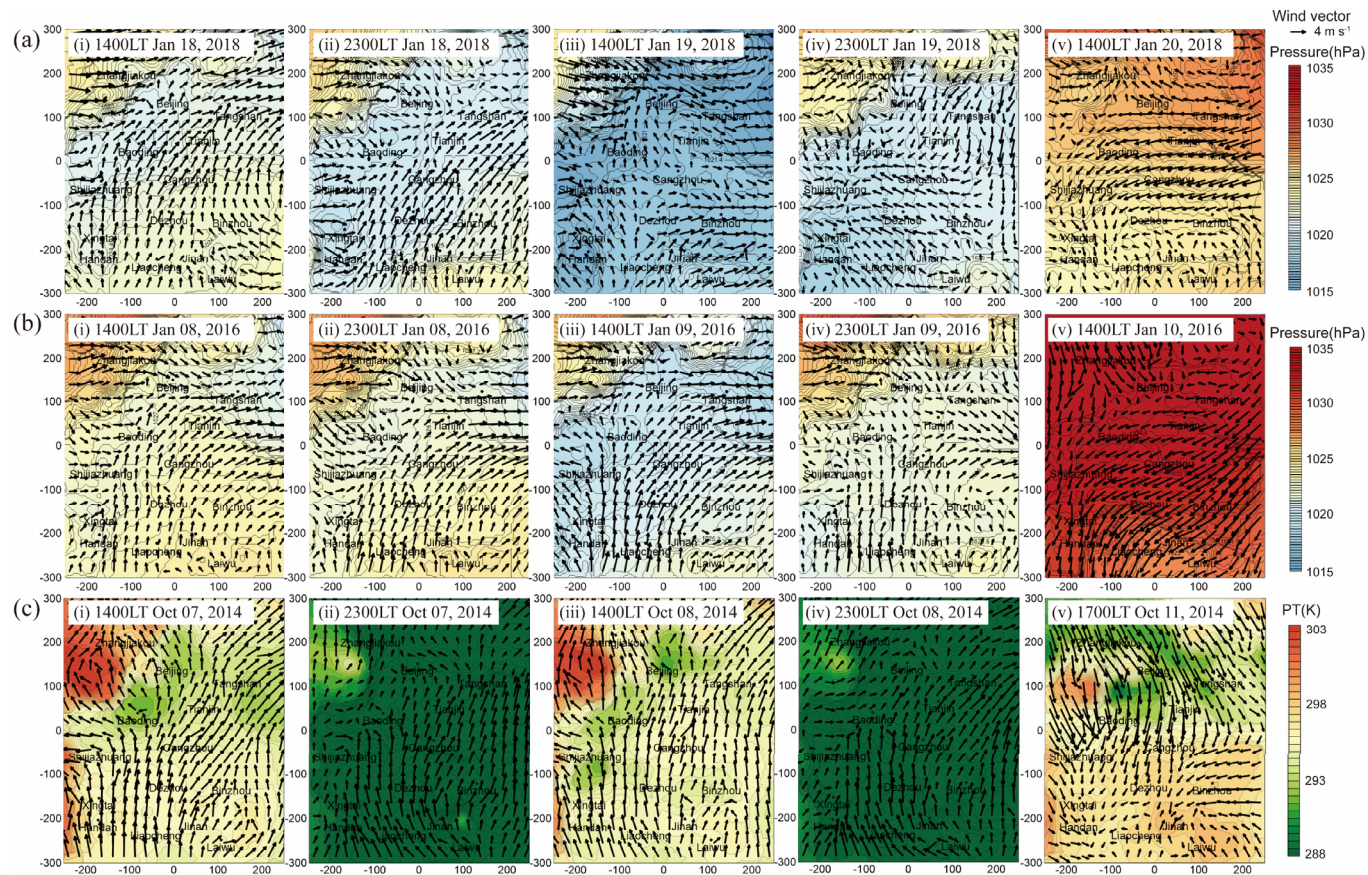
227 Figure 3. Temporal evolution of  $PM_{2.5}$  concentrations during Case1–3, respectively represent (a) west-  
 228 southwest wind shear mode (January 17–21, 2018), (b) south-north wind shear mode (January 7–11,  
 229 2016), and (c) topographic obstruction category (October 7–12, 2014). The locations of these  $PM_{2.5}$   
 230 stations are marked in Fig. 2a.

231 The correspondent surface meteorological fields of the three cases are shown in Fig. 5. Case-1 and  
 232 Case-2 are the two main modes of wind-shear category, for which dynamical AIB plays a dominant role,  
 233 and thus the observed sea level pressure and wind fields are discussed (Fig. 5a-b). Case-3 belongs to the  
 234 topographic obstruction category affected by the AIB created by the cold air damming, and its potential  
 235 temperature and wind fields are displayed to focus on the combined action of the thermal and dynamical  
 236 properties (Fig. 5c). As shown in Fig. 5a, i-iii, the pollution formation and maintenance processes of  
 237 Case-1 were dominated by a leeward trough, which induced the westerly airflow shear to the southwest  
 238 wind and produced a convergence belt at the trough axis. As the trough broadened and moved eastward,  
 239 the wind convergence zone also moved (Fig. 5a, i-iii). On the evening of January 19, 2018, the leeward  
 240 trough temporarily evolved into an inverted trough under the force of the approaching high pressure,  
 241 creating a cyclonic convergence (Fig. 5a, iv). This explains why the heavy pollution expands eastward  
 242 in this episode (refer to Fig. 4a, i-iv). Until January 20, 2018, a high-pressure system invaded the NCP  
 243 from the northeast, bringing strong northeast winds (Fig. 5a, v), which made the pollution disperse to the  
 244 south in turn (refer to Fig. 4a, v). During Case-2, a saddle-shaped pressure field persisted in the pollution  
 245 formation-maintenance stage and induced the prevailing northerly winds in the northern NCP against the



246

247 Figure 4. Spatial distributions of observed surface  $PM_{2.5}$  concentrations (shaded colors) at the pollution stages of (i) formation, (ii-iv) maintenance, and (v) diffusion during  
 248 representative Case1–3 under (a) west-southwest wind shear mode, (b) south-north wind shear mode, and (c) topographic obstruction category. Values shown on x- and y-axis  
 249 denote the distances (km) to the domain center. The  $PM_{2.5}$  concentration fields are derived from spatial interpolation of pollution observed data at monitoring stations.



250

251

Figure 5. Observed sea level pressure/potential temperature and wind vectors at the pollution stages of (i) formation, (ii-iv) maintenance, and (v) diffusion during representative

252

Case1-3 under (a) west-southwest wind shear mode, (b) south-north wind shear mode, and (c) topographic obstruction category. The shaded colors represent the sea level

253

pressure in (a-b) and the potential temperature in (c). The arrows indicate wind vectors. Values shown on x- and y-axis denote the distances (km) to the domain center.

254 dominant southerly flows in the southern area (Fig. 5b, i-iv). As a result, the polluted air mass was  
255 prevented from advancing northward to the mountains, causing a strong contrast in pollution  
256 concentration between the northern and southern parts of the domain (refer to Fig. 4b i-iv). Its pollution  
257 diffusion process was also associated with a northeast high-pressure system, by strong northeasterly  
258 airflows cleaning up the PM<sub>2.5</sub> (Fig. 5b, v). As for the Case-3 under the topographic obstruction category,  
259 there was a narrow area with low potential temperature and weak southerly wind at the foot of the  
260 mountains on the windward side in the daytime, but this feature became fuzzy at night (Fig. 5c, i-iv).  
261 This diurnal variation repeatedly occurred during the formation and maintenance stage, which  
262 corresponded excellently to the day-night difference in pollution distribution (refer to Fig. 4c i-iv). In the  
263 end, the strong flows and cold air bursting like a jet stream through a pathway across Zhangjiakou-  
264 Beijing-Tianjin (Fig. 5c, v), made pollutants begin to be swept out from the northwest (refer to Fig. 4c,  
265 v).

### 266 3.2 Evaluation of simulated meteorological field

267 To reveal the PBL three-dimensional structure of these representative cases, numerical simulations  
268 are conducted using the WRF model. It is necessary to evaluate the model reliability before analyzing  
269 the simulated results. The model-observation comparisons in the previous studies usually focus on the  
270 time series of surface meteorological elements, such as 10 m wind speed and direction, 2 m temperature  
271 and humidity (Rogers et al., 2013; Bei et al., 2018; Qu et al., 2021). The model performance of their  
272 spatial fields is often ignored, and the simulated PBL vertical structure is rarely evaluated. But the  
273 regional distribution and vertical structure of wind, temperature, and humidity are crucial for air pollution.  
274 And of course, the PBL height is a key parameter in characterizing air pollution ventilation conditions.  
275 In this study, the evaluation is carried out from three perspectives: i) the temporal evolution and ii) the  
276 spatial pattern of near-surface potential temperature and wind speed, as well as iii) the vertical-temporal  
277 structure of these two variables at the sounding sites, in addition to the temporal variation of PBL height.

278 For the temporal evolution of the near-surface potential temperature and wind speed, the hourly  
279 observations and simulations of 13 key cities (Beijing, Tianjin, Shijiazhuang, Baoding, Handan,  
280 Tangshan, Cangzhou, Dezhou, Jinan, Weifang, Binzhou, Chengde and Zhangjiakou) evenly distributed  
281 in the NCP are compared during these three pollution cases. The model outputs are extracted from the  
282 grid points nearest to the observed sites. As shown in Table 1, the correlation coefficients of the simulated  
283 and observed hourly evolution of potential temperature and wind speed are 0.80~0.91 and 0.54~0.64  
284 ( $p<0.01$ ), respectively. In order to exclude the influence of the diurnal cycle on the correlation, the daily  
285 averages are also calculated and the obtained correlation coefficients are as high as 0.65~1 and 0.62~1  
286 ( $p<0.01$ ) for potential temperature and wind speed, respectively (Table S1). The statistical results  
287 demonstrate that the major variations in the time series of the surface observations are reproduced well

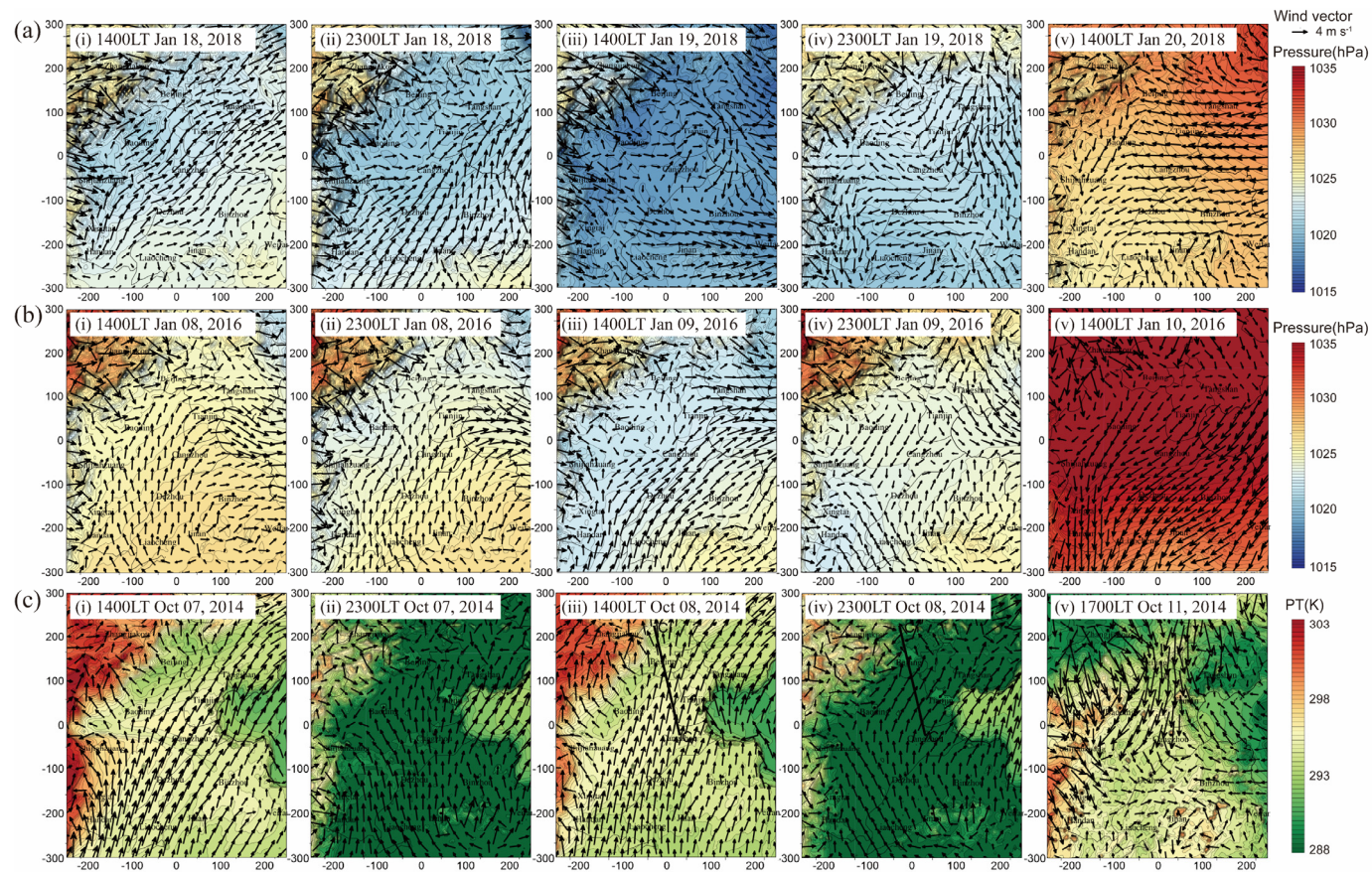
288 by the model, which has also been recognized in previous studies (Rogers et al., 2013; Bei et al., 2018;  
 289 Qu et al., 2021).

290 Table 1. Statistics of model performance for the hourly evolution of near-surface potential temperature  
 291 and 10 m wind speed for selected 13 cities during the representative cases.

	Case-1				Case-2				Case-3			
	PT (K)		WS (m s <sup>-1</sup> )		PT (K)		WS (m s <sup>-1</sup> )		PT (K)		WS (m s <sup>-1</sup> )	
	R	RMSE	R	RMSE	R	RMSE	R	RMSE	R	RMSE	R	RMSE
Beijing	0.80	2.20	0.62	1.15	0.87	2.60	0.61	1.69	0.91	2.20	0.73	1.65
Tianjin	0.89	2.40	0.66	1.48	0.85	1.90	0.63	1.97	0.92	2.10	0.61	2.13
Shijiazhuang	0.77	2.80	0.52	2.02	0.82	2.50	0.66	1.69	0.88	2.20	0.58	1.95
Baoding	0.83	2.50	0.60	1.34	0.85	2.40	0.61	1.53	0.89	2.30	0.60	1.97
Handan	0.93	1.40	0.48	1.36	0.78	3.20	0.56	2.27	0.95	1.30	0.66	1.94
Tangshan	0.69	4.00	0.62	1.44	0.81	3.30	0.53	1.64	0.85	3.00	0.46	2.24
Cangzhou	0.85	3.00	0.64	1.23	0.79	2.50	0.60	1.92	0.94	2.10	0.75	1.45
Dezhou	0.78	3.70	0.51	1.69	0.87	1.50	0.63	2.82	0.90	2.30	0.55	2.97
Jinan	0.76	2.80	0.49	2.96	0.74	2.40	0.63	2.45	0.91	2.10	0.56	3.10
Weifang	0.79	2.10	0.53	1.42	0.78	2.50	0.71	1.99	0.94	2.10	0.85	1.40
Binzhou	0.81	2.50	0.51	1.97	0.83	2.30	0.86	1.29	0.92	2.00	0.81	1.47
Chengde	0.75	5.10	0.47	2.06	0.63	6.50	0.47	2.60	0.84	3.70	0.56	1.74
Zhangjiakou	0.90	5.40	0.33	2.23	0.77	5.30	0.47	3.13	0.96	4.80	0.54	2.50
<b>Average</b>	<b>0.81</b>	<b>3.07</b>	<b>0.54</b>	<b>1.72</b>	<b>0.80</b>	<b>2.99</b>	<b>0.61</b>	<b>2.08</b>	<b>0.91</b>	<b>2.47</b>	<b>0.64</b>	<b>2.04</b>

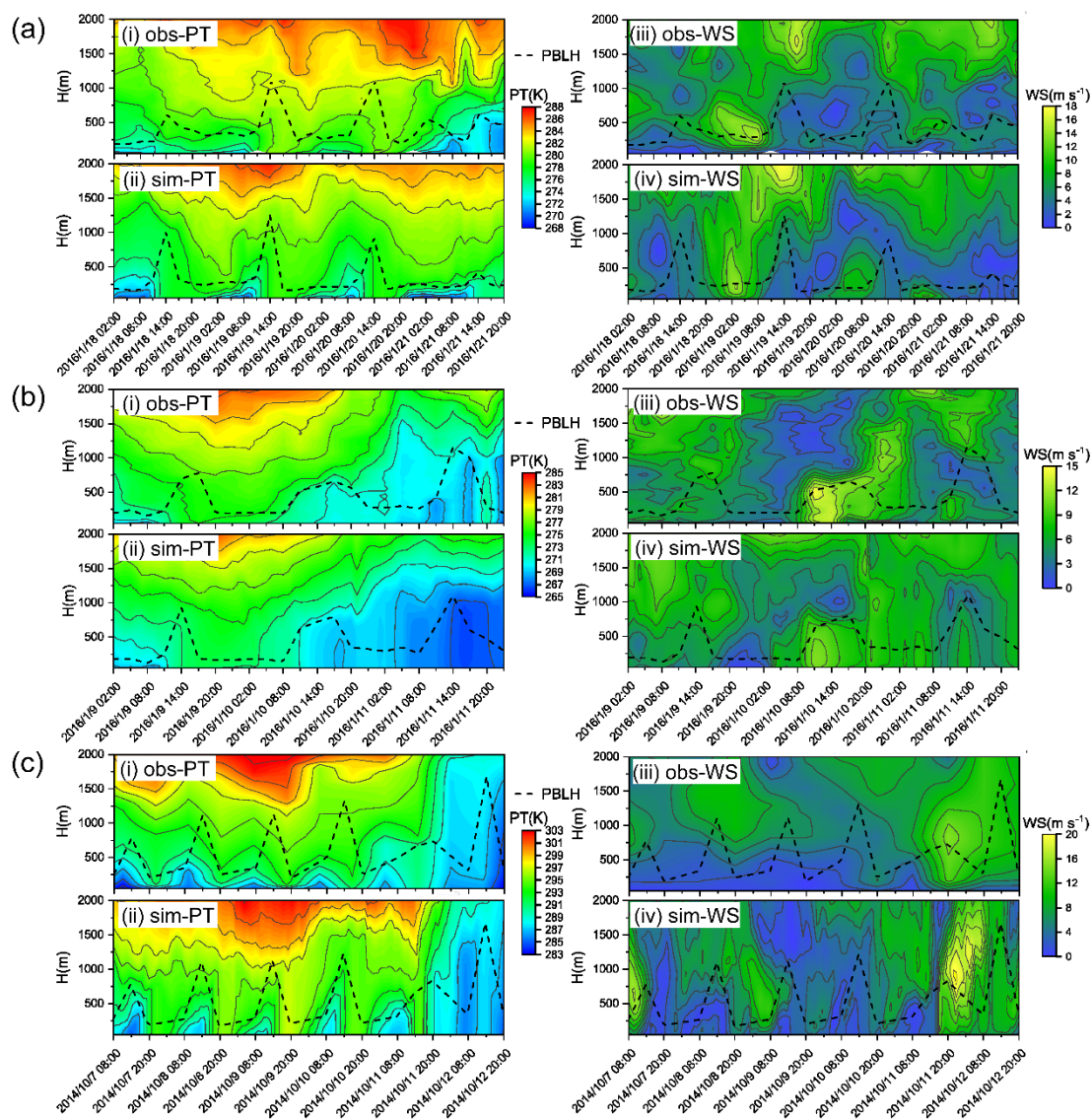
292 Case-1: west-southwest wind shear mode (January 17–21, 2018); Case-2: south-north wind shear mode  
 293 (January 7–11, 2016); Case-3: topographic obstruction category (October 7–12, 2014).

294 Compared with Fig. 5, the simulated surface meteorological fields during the three cases are  
 295 displayed in Fig. 6. In Case-1 and Case-2, the leeward trough and saddle-shaped pressure field, as well  
 296 as the corresponding west-southwest wind shear and south-north wind shear are reproduced in the  
 297 simulated fields (Fig. 6a-b, i-iv vs Fig. 5a-b, i-iv). Also, their movement and evolution during the  
 298 pollution formation-maintenance processes are captured by the WRF model, although there are small  
 299 deviations in the specific positions. At the diffusion stage, the simulated northeastern high-pressure and  
 300 the prevailing easterly/northeasterly winds are comparable with the observed fields (Fig. 6a-b, v vs Fig.  
 301 5a-b, v). As for Case-3, the modeling result of surface meteorological fields successfully reflect the  
 302 narrow cold zone and stagnant wind belt at the foot of the mountains, as well as their diurnal variation  
 303 and sustainability in the pollution formation-maintenance stage (Fig. 6c, i-iv vs Fig. 5c, i-iv). In the  
 304 simulation field, the cold zone is shorter at its south end on the afternoon of October 08, 2014, and there  
 305 is an overestimate of the potential temperature in the northwest mountains and the Bohai Sea at night. At  
 306 the end of this episode, a strong northerly cold airflow similar to the observation appears in the simulation  
 307 field (Fig. 6c, v vs Fig. 5c, v). Generally, the main features of the surface distributions of meteorological  
 308 observations during these three cases are reflected well in the simulated fields.



309

310 Figure 6. Simulated sea level pressure/potential temperature and wind vectors at the pollution stages of (i) formation, (ii-iv) maintenance, and (v) diffusion during representative  
 311 Case1-3 under (a) west-southwest wind shear mode, (b) south-north wind shear mode, and (c) topographic obstruction category. The shaded colors represent the sea level  
 312 pressure in (a-b) and the surface potential temperature in (c). The arrows indicate wind vectors. Values shown on x- and y-axis denote the distances (km) to the domain center.  
 313 Lines  $C_1C_1'$  in (c) refer to the cross-sections of the potential temperature in Fig. 4-12.



314

315 Figure 7. Observed and simulated time-height cross sections of potential temperature (left) and wind  
 316 speed (right) during representative Case1–3 under (a) west-southwest wind shear mode (January 18–21,  
 317 2018), (b) south-north wind shear mode (January 9–11, 2016), and (c) topographic obstruction category  
 318 (October 7–12, 2014). The dashed lines indicate the PBL heights. The observation data in (a-b) and in  
 319 (c) are obtained from intensive sounding experiments and routine soundings, respectively.

320 Moreover, the simulated and observed height-time cross sections of potential temperature and wind  
 321 speed, as well as the PBL height, are compared to reveal the model’s ability to capture the atmospheric  
 322 vertical structure of each case (Fig. 7). The observation data of Case-1 and Case-2 are obtained from  
 323 intensive sounding experiments at the Dezhou site and Cangzhou site, respectively. While the observation  
 324 information during Case-3 is provided by routine soundings at the Beijing site. As for Case-1, the model  
 325 successfully reproduces the thermal structure evolution in the pollution formation-maintenance period,  
 326 while the final uplift of the inversion layer and the growth of PBL are not well captured with an  
 327 underestimation of about 200-300 m (Fig. 7a, i-ii). In comparison, the dynamical structures, the dominant

328 roles in this category, are simulated much better. The vertical location and temporal transition of the  
329 strong and weak wind layers are comparable with observations (Fig. 7a, iii-iv). The correlation  
330 coefficient ( $R$ ) between simulated and observed PBL height is about 0.68 ( $p < 0.01$ ). The model  
331 performance during Case-2 is satisfactory both for cross-sections of the potential temperature and wind  
332 speed. The formation and decay of upper temperature inversion and the development of the cold  
333 convective PBL are consistent between observation and simulation, though there are some  
334 underestimations in the modeled results (Fig. 7b, i-ii). The weak wind layer presented in the maintenance  
335 stage and vertical wind shear that occurred in the diffusion stage are also captured by the model with  
336 smaller gradients (Fig. 7b, iii-iv). Meanwhile, observed and simulated PBL heights show a consistent  
337 evolution with a correlation coefficient as high as 0.78 ( $p < 0.01$ ). Both of their PBL heights are lower  
338 during the pollution formation-maintenance stage and increase by more than 1000 m in the diffusion  
339 stage. In Case-3, the WRF reproduces the observed diurnal cycle of the potential temperature in the low-  
340 level and the continuous warming at the upper layer during the formation-maintenance process, as well  
341 as the replacement of a well-mixed cold air mass in the last phase (Fig. 7c, i-ii). The evolution of the  
342 simulated wind speed is roughly similar to the observation, including the maintenance of the calm wind  
343 layer in the first four days and the appearance of the final strong wind layer (Fig. 7c, iii-iv).  
344 Correspondingly, the PBL height is characterized by typical diurnal variations during the polluted period,  
345 and begins to abruptly develop in the evening of October 12, 2014, associated with the cold air mass and  
346 strong wind, both in observation and simulation ( $R = 0.81$ ,  $p < 0.01$ ). Even so, there are some  
347 inconsistencies in the details of observation and simulation evolution, which may result from the coarse  
348 resolution of routine soundings in time and vertical direction, in addition to the uncertainties of model  
349 simulation.

350 Overall, the model shows the ability to capture the observed mesoscale systems and atmospheric  
351 thermal-dynamical structures reasonably both at the surface and in the vertical direction. With confidence  
352 in the model results, we now proceed to a detailed investigation of the PBL spatial structure affected by  
353 mesoscale AIBs under various pollution categories.

### 354 **3.3 PBL spatial structure**

355 We analyze the simulated vertical cross-sections of the mesoscale systems and AIBs to reveal the  
356 three-dimensional structure of the PBL. Two key parameters, potential temperature and wind divergence,  
357 are used to respectively indicate the atmospheric thermal stability and dynamical convergence, in  
358 addition to another important parameter: the PBL depth. They directly affect the vertical mixing and  
359 horizontal transport of  $PM_{2.5}$ , and are critical for pollution formation and distribution.

#### 360 **Wind shear category**

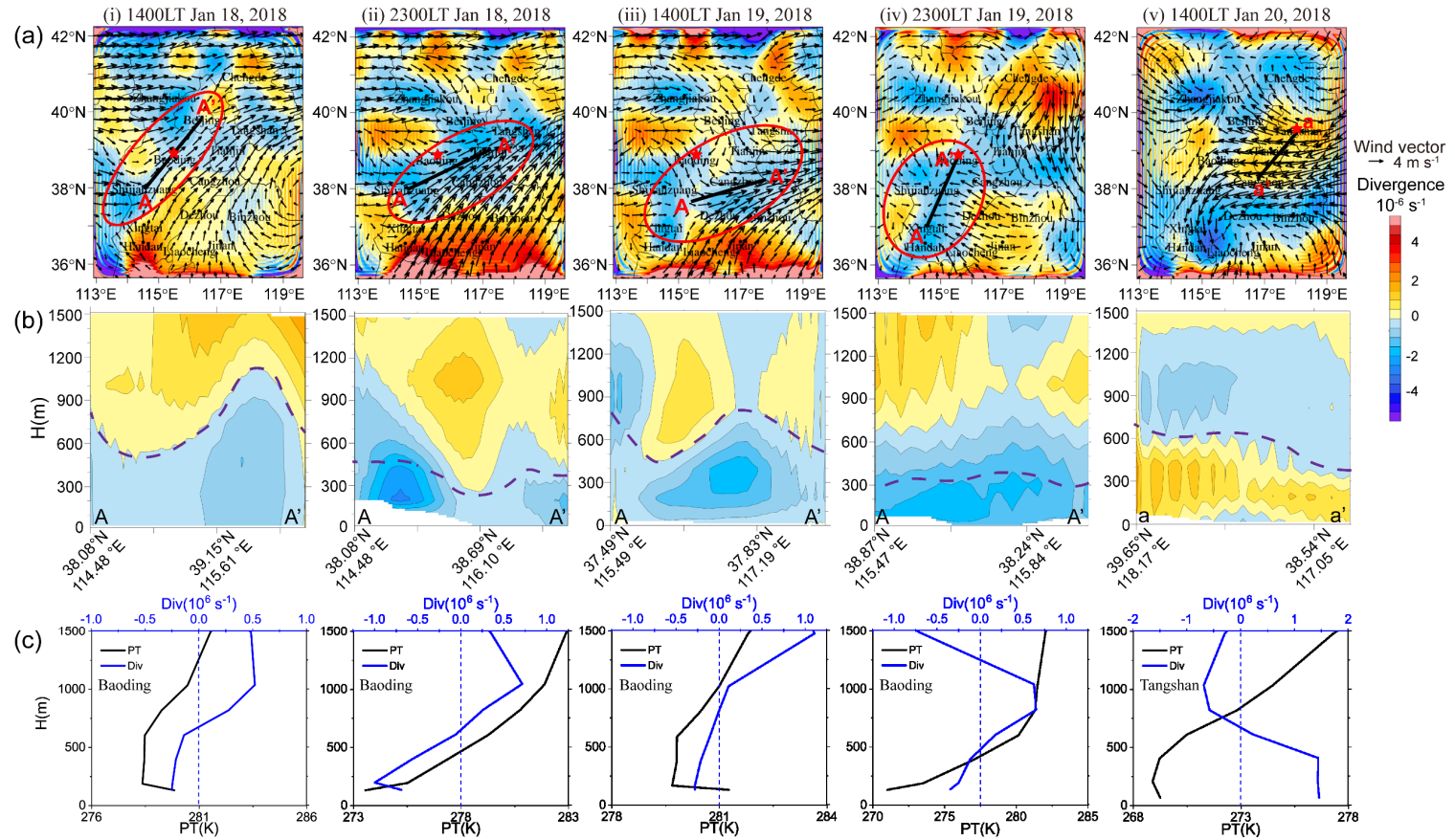
361 This pollution category, mainly involving two modes of west-southwest wind shear and south-north



362 wind shear, is driven by dynamical flows. Therefore, for the corresponding Case-1 and Case-2, the wind  
363 divergence sections are analyzed in detail in the following (Figs. 8-9). The potential temperature sections  
364 are presented in the supplementary material (Figs. S2-3), which illustrates that there is no significant  
365 thermal discontinuity.

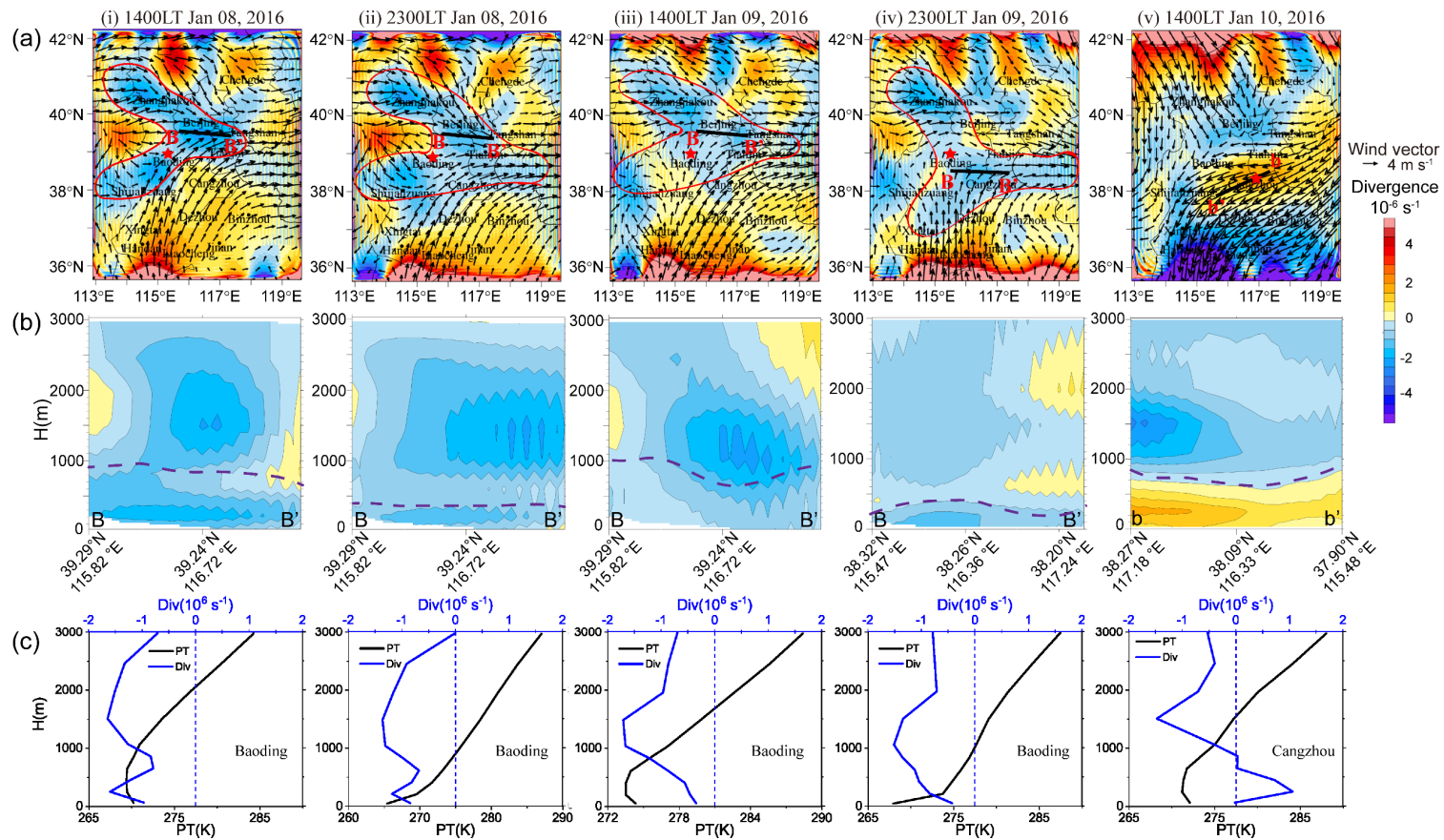
366 Figure 8 displays the PBL dynamical structure of Case-1. During the pollution formation-  
367 maintenance stage, with the establishment of a low-pressure trough (refer to Fig. 6a), westerly winds  
368 shifted to southwesterly winds at the trough axis and thus formed a convergence belt at the surface with  
369 a divergence of  $-2\sim-4\times 10^{-6} \text{ s}^{-1}$  (Fig. 8a, i). As a consequence, a mass of pollutants were transported  
370 here and further accumulated to form a pollution zone (refer to Fig. 4a, i). This trough-convergence belt  
371 continued to move to the east, and evolved into a cyclonic-convergence center at the end of the  
372 maintenance phase (Fig. 8a, i-iv). During this process, its affected area was expanded, so that the large  
373 range of NCP was filled with pollutants (refer to Fig. 4a, ii-iv). The vertical section across the surface  
374 convergence belt shows that the depth of the convergence layer did not exceed 1000 m, with a  
375 compensating divergence layer immediately above it, being consistent with the evolution of the PBL (Fig.  
376 8b, i-iv). Furthermore, the vertical profiles of the wind divergence and potential temperature at the  
377 Baoding site located in the convergence belt are extracted to illustrate the PBL dynamical structure more  
378 clearly. It shows that the mutation of divergence value and the jump of potential temperature roughly  
379 appeared at the same height (Fig. 8c, i-iv), which demonstrated the vertical scale of the wind convergence  
380 belt was equivalent to the depth of the PBL. This phenomenon reveals that the west-southwest wind shear  
381 convergence caused by the trough mainly occurred within the PBL, reflecting its mesoscale property. In  
382 the process of pollution diffusion, with the advent of a northeast high-pressure system, divergent wind  
383 fields occurred correspondently (Fig. 8a, v), which made this part of the pollutants cleaned quickly (refer  
384 to Fig. 4a, v). The vertical cross-section of this divergent layer and vertical profiles at the Tangshan site  
385 show that the northeast wind divergence layer was relatively thin with a thickness of no more than 600  
386 m (Fig. 8b-c, v), implying that the removal of pollutants only occurred within the PBL.

387 As for the south-north wind shear mode, the surface divergence fields displayed a "lying Y shaped"  
388 convergence zone with the opening to the west during the pollution formation-maintenance stage of  
389 Case-2 (Fig. 9a, i-iv), which was caused by the meeting of the southerly winds and the northerly winds  
390 and then turning to the easterly winds. This convergence mode made the distribution of pollutants in a  
391 pattern of much higher concentration in the south and lower in the north, with a clear edge between these  
392 two air masses (refer to Fig. 4b, i-iv). Although the southerly winds in the southern NCP kept the  
393 pollutants transported northward, they never reached the northernmost part due to the opposite airflow  
394 there. The vertical cross-sections of this special convergence zone exhibited a depth extending upwards  
395 for more than 3000 m, with a peak between 1000 m and 2000 m above the PBL top (Fig. 9b, i-iv).  
396 Referring to the vertical profiles of wind divergence and potential temperature at the Baoding site, it can



397

398 Figure 8. (a) Surface spatial distributions, (b) vertical cross-sections and (c) vertical profiles of the simulated wind divergence at the pollution stages of (i) formation, (ii-iv)  
 399 maintenance, and (v) diffusion during representative Case-1 under west-southwest wind shear mode. The red ellipses, black lines, and red stars in (a) indicate the convergence  
 400 belt, the section lines in (b), and the profile sites in (c), respectively. The purple dashed lines in (b) indicate the PBL heights. The potential temperature profiles are presented  
 401 in (c) to indicate the boundary layer top at the representative sites.



402

403

404

405

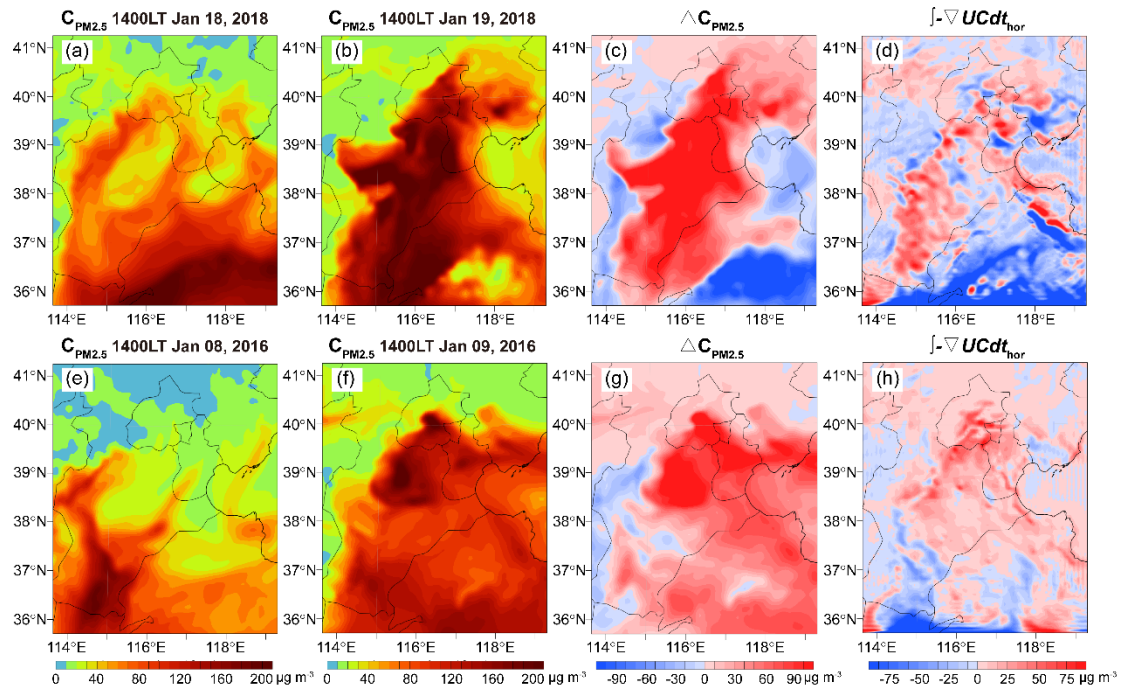
Figure 9. Same as Fig. 8, but for representative Case-2 under south-north wind shear mode. The red lying-Y shapes, black lines, and red stars in (a) indicate the convergence belt, the section lines in (b), and the profile sites in (c), respectively. The purple dashed lines in (b) indicate the PBL heights. The potential temperature profiles are presented in (c) to indicate the boundary layer top at the representative sites.

406 be seen that the depth of the convergence layer far exceeded the height of the PBL, whether it was in the  
407 daytime or at night (Fig. 9c, i-iv). These phenomena demonstrate that the south-north wind shear created  
408 by the saddle-shaped pressure field is of much larger vertical and horizontal scales. The dynamical  
409 feature was no longer limited to the PBL, but extended to the sub-synoptic scales. In the pollution  
410 diffusion stage of this case, the PBL structure was the same as in Case-1 (Fig. 9a-c, v), and has been  
411 described in the above paragraph.

412 To provide explicit support to the above explanation between the dynamical convergence feature  
413 and the pollution development, we adopt a chemical transport model (WRF-Chem) to simulate the PM<sub>2.5</sub>  
414 pollution process and directly quantify the advection term in the PM<sub>2.5</sub> concentration prognostic equation,  
415 i.e.:

$$416 \quad \frac{\partial c}{\partial t} = -\nabla \cdot (\vec{U}c)_{adv} + \nabla \cdot (K_e \nabla c)_{diff} + E_{emiss} + S_{sink} + R_{chem}, \quad (1)$$

417 where  $c$  is PM<sub>2.5</sub> concentration,  $\vec{U}$  is the wind vector,  $K_e$  is the turbulent diffusion coefficient. The  
418 first term on the right side of the equation represents the advection process both horizontally and  
419 vertically. The second term is turbulent diffusion, and the last three terms represent emissions, deposition  
420 and chemical reactions, respectively. The present study pays attention to the horizontal advection, which  
421 is considered of most important effect on the pollution development for the wind shear category. Details  
422 of the model configuration and validation are described in the supplementary material (Text S1, Fig. S4,  
423 and Table S2). The simulations of Case-1 and Case-2 well reproduce the PM<sub>2.5</sub> pollution concentration  
424 patterns and their evolution. Their pollution formation and maintenance stages are discussed here. For  
425 Case-1, the simulated near-surface PM<sub>2.5</sub> fields at 14:00 of both January 18 and January 19, 2018, as well  
426 as their difference are displayed in Fig. 10a-c, indicating that the air pollution aggravates and spreads  
427 eastward. The temporal integration of the PM<sub>2.5</sub> horizontal advection term over this period (Fig. 10d)  
428 agrees well with the concentration increment pattern in Fig. 10c, demonstrating the crucial role of the  
429 dynamical convergence in the development of PM<sub>2.5</sub> pollution. The contribution of the horizontal  
430 advection term on the total increment of PM<sub>2.5</sub> concentration during this period over most of this region  
431 is very high, e.g., at Handan, Shijiazhuang, Baoding, and Tianjin, the contribution ranges 40%-85%. For  
432 Case-2, heavy pollution is transferred to the north and east from January 08 to January 09, 2016 (Fig.  
433 10e-g). Similar to Case-1, the advection term integrated over the pollution formation-maintenance period  
434 (Fig. 10h) presents good agreement with the PM<sub>2.5</sub> increment pattern (Fig. 10g). Quantitatively, this term  
435 contributes to total concentration accumulation as high as 27%-80% in the pollution process, especially  
436 in Beijing, Tianjin, and Baoding. This result is also consistent with those in previous works (Jiang et al.,  
437 2015; Chang et al., 2019; Jin et al., 2020). The above analysis indicates that, the airflow convergence  
438 AIB does not sharply confine the pollution air mass, but provides a circumstance or structure for  
439 pollutants transporting/accumulating along or nearby this zone. Because of the dynamical property, the  
440 concentration fields of the wind shear category pollution are more variable in space and time.



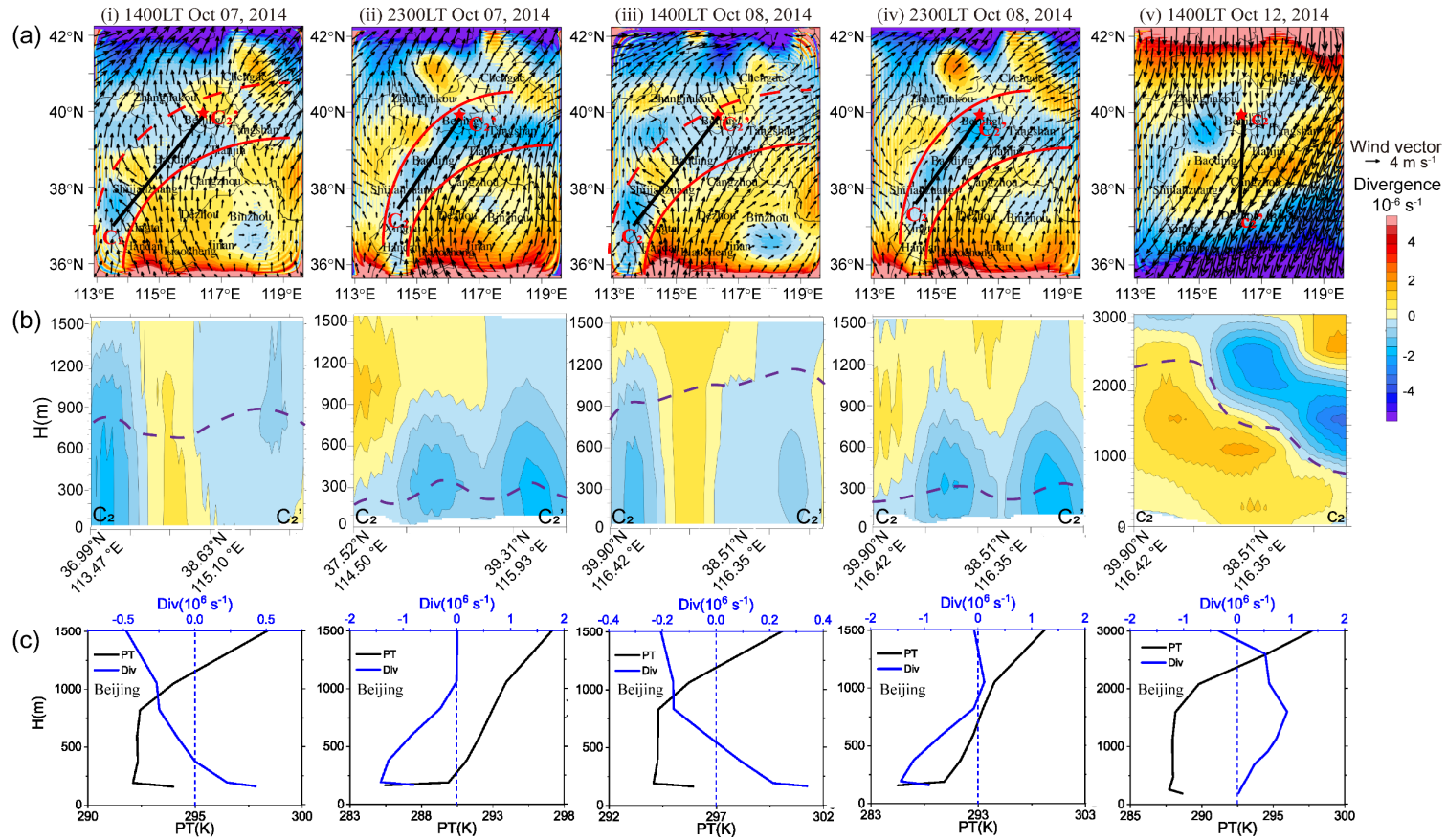
441

442 Figure 10. Simulated (a-b, e-f) near-surface  $PM_{2.5}$  concentrations at two instants during the pollution  
 443 formation-maintenance stage and (c, g) their difference, as well as (d, h) the temporal integration of the  
 444  $PM_{2.5}$  horizontal advection term over this stage for Case-1 (upper) and Case-2 (lower).

445 **Topographic obstruction category**

446 As an outcome of a mixture of the thermal and dynamical effects, the topographic obstruction  
 447 category pollution is analyzed from the perspectives of both the wind divergence and potential  
 448 temperature to reveal the dynamical and thermal structure of the PBL.

449 Figure 1011 shows the dynamical characteristics of the PBL during Case-3. In the pollution  
 450 formation-maintenance stage, there was an arc-shaped convergence belt at the foot of the mountains on  
 451 the windward, due to the momentum loss in the northward flow under the action of topographic  
 452 obstruction (Fig. 1011a, i-iv). The shape of this convergent belt was more regular at night (Fig. 1011a, ii,  
 453 iv) but had some breakages at the northern edge during the day when there was a local southeast wind  
 454 around Beijing and Shijiazhuang (Fig. 1011a, i, iii). The vertical sections also displayed the general  
 455 features and diurnal difference, showing an integral convergence layer at night with a depth of the  
 456 mountain height (Fig. 1011b, ii, iv), and an isolated divergent layer emerged during the daytime (Fig.  
 457 1011b, i, iii). The vertical profiles of the wind divergence and potential temperature at Beijing were  
 458 further shown in Fig. 1011c, i-iv. In the evening, the atmosphere below 1200 m was convergent with the  
 459 peak appearing near the surface of about  $-1.5 \times 10^{-6} \text{ s}^{-1}$ . In the afternoon, there was a weak divergence  
 460 layer with a strength of about  $0.5 \times 10^{-6} \text{ s}^{-1}$  and a thickness of about 200~300 m within the PBL. We infer  
 461 that the day-night variation may be the consequence of the mountain-valley circulation, since the  
 462 northwestward daytime valley wind developed along the mountain gorges near Beijing and Shijiazhuang



463

464

Figure 1011. Same as Fig. 8, but for representative Case-3 under the topographic obstruction category. The red curves, black lines, and red stars in (a) indicate the convergence

465

belt, the section lines in (b), and the profile sites in (c), respectively. The purple dashed lines in (b) indicate the PBL heights. The potential temperature profiles are presented

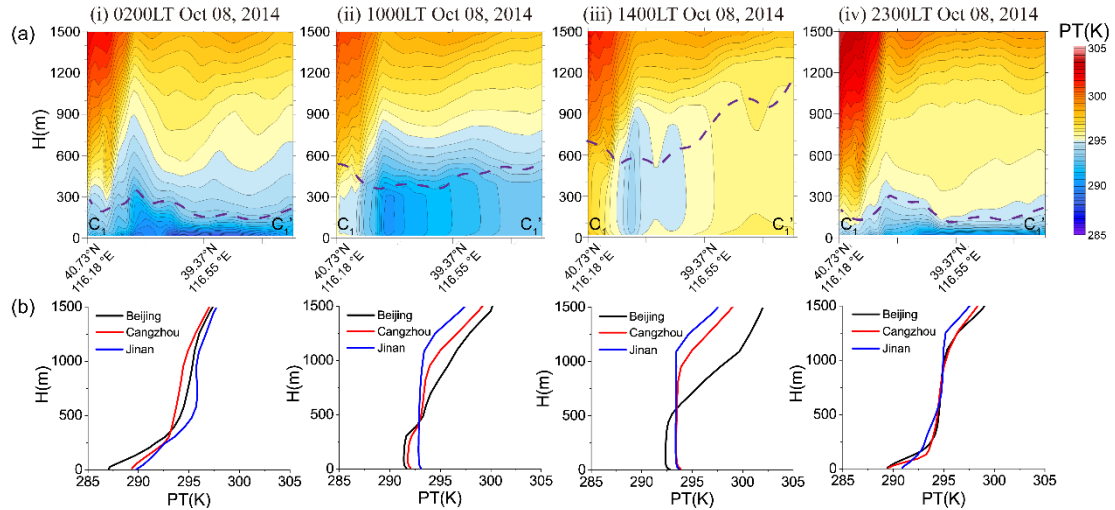
466

in (c) to indicate the boundary layer top at the representative sites.

467 leading to flow divergence, and downslope winds formed at night strengthening the surface convergence.  
468 During the pollution diffusion stage, the northern part of the domain was in a strong divergence condition  
469 (Fig. 4011a, v). The corresponding cross-section shows that the north wind divergence layer was very  
470 deep (nearly 3000 m), even extending beyond the boundary layer. It gradually thins from north to south  
471 with the decrease of the PBL height (Fig. 4011b, v). Moreover, the vertical profiles of the divergence and  
472 potential temperature at the Beijing site show that the PBL was well developed up to 2000 m,  
473 accompanied by strong horizontal divergence throughout the layer (Fig. 4011c, v). Both of them indicate  
474 extremely favorable ventilation conditions.

475 The thermal properties and their evolution, especially diurnal variation, play an important role in  
476 this pollution pattern, which has been presented in the above surface analysis. Hence, we further explore  
477 the three-dimension thermal structure of the PBL, taking the vertical cross-sections of potential  
478 temperature across the characteristic cold area in the pollution maintenance stage (October 8, 2014, the  
479 location of the cross-section is shown in Fig. 6c) as an illustration. In the early hours of the morning,  
480 although there were surface inversions across the whole region, the cold air masses in front of the  
481 mountains were much thicker (Fig. 412a, i). After sunrise, the convective boundary layer developed  
482 both in the front of the mountains and in the plain due to the surface heating, but the temperature in the  
483 southern plain was higher and the PBL was slightly deeper (Fig. 412a, ii). In the afternoon, a deep, well-  
484 mixed warm PBL (with a height of more than 1000 m) has formed in the southern plain while a cold air  
485 mass capped by strong inversion (at the height of about 600-1000 m) still remained in the northern area  
486 (Fig. 412a, iii). At night, large amounts of cold air accumulated at the foot of the mountains again (Fig.  
487 412a, iv). The vertical profiles of the simulated potential temperature of the three cities from south to  
488 north, Jinan, Cangzhou and Beijing, also support this thermal evolution process. At 0200 LT, there were  
489 surface inversions at all three cities, and Beijing had the strongest inversion intensity of about 2 K per  
490 100 m (Fig. 412b, i). By 1000 LT, the PBL height in Jinan had increased to 1100 m, while the convective  
491 boundary layers in Beijing and Cangzhou were shallow (about 400 m, Fig. 412b, ii). In the afternoon,  
492 the PBL was fully developed with the height from the south to the north ranging from 1150 m to 650 m,  
493 and there was still a thick inversion layer above Beijing (Fig. 412b, iii). At 2300 LT, the surface inversion  
494 at the three sites has formed again (Fig. 412b, iv). The persistent cold air mass in front of the mountains  
495 is similar to the cold air damming on the eastern side of the Appalachian (Bell and Bosart, 1988). The  
496 prevailing southerly warm airflows were blocked by the mountains and the geostrophic balance was  
497 disrupted, so that the heat cannot reach the foothills and the air was further cooled due to the turning  
498 easterly wind. Meanwhile, the air mass accumulated and ascended with adiabatic cooling in front of the  
499 mountains. It should be noted that the southeast edge of this cold area was more pronounced during the  
500 daytime (Fig. 5c, Fig. 412), in comparison to that at night. This is reasonable given that the nocturnal  
501 boundary layer was stable over the whole domain and more susceptible to the local property, such as

502 surface heterogeneity, meandering motions, and gravity waves (Mahrt, 1998). Although the AIB was  
 503 relatively unclear at the surface during nighttime, the nocturnal cold layer at the foothills was deeper than  
 504 the southern plain area, probably due to the cold drainage flows along the sidewall of the mountains to  
 505 form a cold air pool. This diurnal cycle of the PBL thermal structure can well explain the day-night  
 506 difference in pollution distribution pattern (refer to Fig. 4e).



507

508 Figure 4. (a) Vertical cross-sections and (b) vertical profiles of the simulated potential temperature at  
 509 (i) 0200 LT, (ii) 1000 LT, (iii) 1400 LT and (iv) 2300 LT on October 08, 2014 in Case-3 under the  
 510 topographic obstruction category. The cross-sections along the line  $C_1C_1'$  are shown in Fig. 6c, iii, iv.  
 511 The purple dashed lines in (a) indicate the PBL heights.

#### 512 4 Summary and discussion

513 This study investigated the three-dimensional PBL structures modified by mesoscale AIBs under  
 514 various pollution categories by using the mesoscale meteorological model WRF. Based on the  
 515 classification of pollution episodes in the NCP (Jin et al., 2022 submitted), representative pollution cases  
 516 of the wind shear category and orographic obstruction category were analyzed. The WRF model was  
 517 comprehensively evaluated for its reliability, by comparison with observed PBL vertical structure, as  
 518 well as the temporal series and spatial distribution of the surface meteorological fields. The evolution of  
 519 the PBL spatial structures and their interaction with the mesoscale AIBs during the pollution episodes  
 520 were fully revealed, from both thermal and dynamical perspectives.

521 The results of this paper, together with a previous systematic classification study (Jin et al., 2022  
 522 submitted) and a detailed case study for frontal category (Jin et al., 2021), depict a more complete and  
 523 clearer view of the PBL spatial structures during pollution episodes in the regional scale of NCP (as  
 524 schematically shown in Fig.1). All the pollution conditions during the autumn and winter were classified  
 525 into three categories. The most prominent was the frontal category. With an isolated cold air mass



526 laterally bounded by the warm frontal AIB on one side and mountains on another side, the PBL was  
527 vertically suppressed by a dome-like warm cap. Typically, the intensity of the frontal inversion can be as  
528 large as 3~6 K per 100 m. As a consequence, the PBL in this cold area was very shallow (as low as  
529 200~300 m) and kept stable stratification, in sharp contrast to the deep and well-mixing boundary layer  
530 outside this zone (Fig. 1a). This explained why PM<sub>2.5</sub> accumulated rapidly in this enclosed and stable  
531 space and formed a laterally clearly defined polluted air mass. Diurnally, the nocturnal PBL in this  
532 category was less typical than its daytime counterpart. The thermal structure of the PBL played a leading  
533 role in this category, resulting in the most severe pollution level.

534 The wind shear category, with two main modes: west-southwest wind shear and south-north wind  
535 shear, was featured with airflow convergence AIB and dominated by dynamical processes. The first mode  
536 was characterized by a low-pressure trough. A convergence layer lay in the wind shear zone with the  
537 thickness of the PBL depth (Fig. 1b), and a typical near-surface divergence of  $-2\sim-4\times 10^{-6} \text{ s}^{-1}$ . It is  
538 accompanied by a compensating divergence layer above the PBL, reflecting the mesoscale property of  
539 the trough AIB. The latter mode displayed a "lying Y shaped" convergence layer from the surface  
540 extending upwards to about 3000 m, with a convergence peak above the PBL top (not shown in Fig. 1).  
541 This implied the sub-synoptic scale features. In this category of both modes, the boundary layer was  
542 dominated by dynamical convergence effects, which resulted in pollutants transport and accumulation,  
543 and thus drove the variation of the PM<sub>2.5</sub> distribution. It corresponded to relatively light pollution in the  
544 NCP.

545 The topographic obstruction pollution category was characterized by a cold air damming AIB at the  
546 foot of the windward side of the mountains. It usually occurred when the southerly winds were too weak  
547 to cross the terrain barrier and the northward flows were blocked. In response, the geostrophic balance  
548 was adjusted, which made the southerly warm advection weaken and further turned to easterly cold  
549 advection. All these factors allowed air masses to accumulate and ascend with adiabatic cooling at the  
550 foothills. The PBL air was cold and capped by a strong inversion in the damming area, in contrast with  
551 well-mixed warm PBL in the southern plain. Meanwhile, the air flows were convergent in front of the  
552 mountains. These general characteristics are shown in Fig. 1c. In more detail, the thermal discontinuity  
553 became indistinct at night due to the surface inversion over the whole domain, while the nocturnal wind  
554 convergence belt was more pronounced. The diurnal variation of the PBL dynamical and thermal  
555 structure made the pollutants concentrate at the foot of the mountains during the daytime while local  
556 pollution formed throughout the entire plain at night.

557 The present study focuses on the characteristic of mesoscale PBL structures under pollution  
558 conditions, and emphasizes their role in shaping regional pollution patterns. The analysis of pollution  
559 evolution is based on the PM<sub>2.5</sub> concentration fields interpolated or diagnosed from monitoring data,  
560 relying on densely distributed stations. However, the PBL spatial structure is presented by numerical

561 simulation, due to the scarcity and limitation of sounding data. Evaluation from the spatial-temporal  
562 variation of the surface meteorological field and PBL vertical structure indicates that the model  
563 performance is good. WRF can capture mesoscale systems and AIBs, as well as their overall evolution  
564 process and diurnal variation. It should be noted that, it is still difficult to reproduce the precise timing  
565 of the buildup and breakup as well as the exact location and range of these systems. This deficiency  
566 should be concerned seriously when simulated meteorological fields are used to drive air quality models,  
567 since a small position bias and time deviation of the AIBs can significantly alter pollution levels at a  
568 certain site (Seaman, 2000; McNider and Pour-Biazar, 2020). Accurate capture of mesoscale AIBs is a  
569 necessary prerequisite for reliable simulation of pollution evolution. Besides, successful reproduction  
570 and forecast of air quality by the chemical transport models also involve other factors, such as the  
571 accuracy of source inventories and the complexity of chemical mechanisms (Travis et al., 2016; Bouarar  
572 et al., 2019; Wang et al., 2021), which are beyond the scope of this study. ~~The aim of the present work is  
573 to provide a clear cognition of these typical PBL structures reproduced by the mesoscale meteorology  
574 model. This goal is achieved satisfactorily.~~ Keeping all these in mind, we conducted supplementary  
575 chemical transport simulations and explicitly demonstrated the role of the airflow convergence AIB in  
576 the formation of wind shear category pollution.

577 At last, the pollution categories presented in this study can still be rough or oversimplified, and the  
578 real processes may be more complex and atypical as analyzed. However, this work, to the authors'  
579 knowledge, is the first trial to reveal the various PBL structures over the vast scale of the NCP, and to  
580 clarify their role in regional PM<sub>2.5</sub> pollution. Modulation of the PBL by mesoscale meteorological  
581 processes, particularly the AIBs, is clearly demonstrated. Extending the view of the PBL from local  
582 vertical properties to mesoscale three-dimension structures may be a step toward a better understanding  
583 of the meteorological effects on regional-scale PM<sub>2.5</sub> pollution.

584

#### 585 **Data availability**

586 The data in this study are available from the corresponding author ([xhcai@pku.edu.cn](mailto:xhcai@pku.edu.cn)).

#### 587 **Author contribution**

588 XHC and XPJ designed the research. MYY and HSZ collected the data. XPJ performed the simulations  
589 and wrote the paper. XHC reviewed and commented on the paper. YS, XSW and TZ participated in the  
590 discussion of the article.

#### 591 **Competing interests**

592 The authors declare that they have no conflict of interest.

593 **Acknowledgements**

594 The authors appreciate the anonymous reviewers for the critical comments that have helped improve this  
595 manuscript. This work was supported by National Key Research and Development Program of China  
596 (2018YFC0213204).

597 **References**

- 598 Baumann, K., Maurer, H., Rau, G., Piringer, M., Pechinger, U., Prevot, A., Furger, M., Neininger, B. and  
599 Pellegrini, U.: The influence of south Foehn on the ozone distribution in the Alpine Rhine valley -  
600 results from the MAP field phase, *Atmos. Environ.*, 35(36), 6379-6390, doi:10.1016/s1352-  
601 2310(01)00364-8, 2001.
- 602 Bei, N. F., Zhao, L. N. Wu, J. R., Li, X., Feng, T. and Li, G. H.: Impacts of sea-land and mountain-valley  
603 circulations on the air pollution in Beijing-Tianjin-Hebei (BTH): A case study, *Environ. Pollut.*, 234,  
604 429-438, doi:10.1016/j.envpol.2017.11.066,2018.
- 605 Bell, G. D. and Bosart, L. F.: Appalachian cold-air damming. *Mon. Wea. Rev.*, 116, 137–161,  
606 doi:10.1175/1520-0493(1988)116,0137:ACAD.2.0.CO;2, 1988.
- 607 Berger, B. W. and Friehe, C. A.: Boundary-layer structure near the cold-front of a marine cyclone during  
608 “ERICA”, *Bound.-Layer Meteor.*, 317-317, doi:10.1007/BF0071125874, 1995.
- 609 Bluestein, H. B.: Surface boundaries of the Southern Plains: Their role in the initiation of convective  
610 storms, in: *Synoptic-dynamical meteorology and weather analysis and forecasting: a tribute to Fred*  
611 *Sanders*, edited by Bosart, L.F., Bluestein, H.B., American Meteorological Society, Boston, pp5-33,  
612 2008.
- 613 Bianco, L., Djalalova, I. V., King, C. W., and Wilczak, J. M.: Diurnal Evolution and Annual Variability  
614 of Boundary-Layer Height and Its Correlation to Other Meteorological Variables in California's  
615 Central Valley, *Bound.-Layer Meteor.*, 140, 491-511, doi:10.1007/s10546-011-9622-4, 2011.
- 616 Bouarar, I., Brasseur, G., Petersen, K., Granier, C., Fan, Q., Wang, X.M., Wang, L.L., Ji, D. S., Liu, Z.R.,  
617 Xie, Y., Gao, W., and Elguindi, N.: Influence of anthropogenic emission inventories on simulations  
618 of air quality in China during winter and summer 2010. *Atmos. Environ.* 198, 236–256.  
619 doi:10.1016/j.atmosenv.2018.10.043, 2019.
- 620 Boutle, I. A., Beare, R. J., Belcher, S. E., Brown, A. R., and Plant, R. S.: The Moist Boundary Layer  
621 under a Mid-latitude Weather System, *Bound.-Layer Meteor.*, 134, 367-386, doi:10.1007/s10546-  
622 009-9452-9, 2010.
- 623 **Chang, X., Wang, S.X., Zhao, B., Xing, J., Liu, X.X., Wei, L., Song, Y., Wu, W.J., Cai, S.Y., Zheng, H.T.,**  
624 **Ding, D. and Zheng, M.: Contributions of inter-city and regional transport to PM<sub>2.5</sub> concentrations**  
625 **in the Beijing-Tianjin-Hebei region and its implications on regional joint air pollution control, *Sci.***

626 [Total Environ. 660, 1191-1200, doi:10.1016/j.scitotenv.2018.12.474, 2019.](#)

627 De Wekker, S. F. J.: Observational and numerical evidence of depressed convective boundary layer  
628 heights near a mountain base, *J. Appl. Meteorol. Climatol.*, 47, 1017-1026,  
629 doi:10.1175/2007jamc1651.1, 2008.

630 Dupont, J. C., Haeffelin, M., Badosa, J., Elias, T., Favez, O., Petit, J. E., Meleux, F., Sciare, J., Crenn, V.,  
631 Bonne, J. L.: Role of the boundary layer dynamics effects on an extreme air pollution event in Paris.  
632 *Atmos. Environ.*, 141, 571–579, doi:10.1016/j.atmosenv.2016.06.061, 2016.

633 Emeis, S., and Schafer, K.: Remote sensing methods to investigate boundary-layer structures relevant to  
634 air pollution in cities, *Bound.-Layer Meteor.*, 121, 377-385, doi:10.1007/s10546-006-9068-2, 2006.

635 Garratt, J. R: *The Atmospheric Boundary Layer*. Cambridge University Press, Cambridge, 1992.

636 Garratt, J. R.: The internal boundary-layer-A review, *Bound.-Layer Meteor.*, 50, 171-203,  
637 doi:10.1007/bf00120524, 1990.

638 Hane, C. E., Rabin, R. M., Crawford, T. M., Bluestein, H. B. and Baldwin, M. E.: A case study of severe  
639 storm development along a dryline within a synoptically active environment. Part II: Multiple  
640 boundaries and convective initiation. *Mon. Wea. Rev.*, 130, 900–920, doi: 10.1175/1520-  
641 0493(2002)130<0900:ACSOSS>2.0.CO;2,2002.

642 Hanna, S. R. and Yang, R.: Evaluations of mesoscale models' simulations of near-surface winds,  
643 temperature gradients, and mixing depths. *J. Appl. Meteorol.* 40 (6):1095–104, doi:10.1175/1520-  
644 0450(2001)040<1095:EOMMSO>2.0.CO;2, 2001.

645 [Jiang, C., Wang, H., Zhao, T., Li, T., Che, H.: Modeling study of PM2.5 pollutant transport across cities  
646 in China's Jing–Jin–Ji region during a severe haze episode in December 2013. \*Atmos. Chem. Phys.\*  
647 15, 2969–2983, doi:10.5194/acp-15-5803-2015, 2015.](#)

648 Jimenez, P. A., de Arellano, J. V. G., Dudhia, J., and Bosveld, F. C.: Role of synoptic- and meso-scales  
649 on the evolution of the boundary-layer wind profile over a coastal region: the near-coast diurnal  
650 acceleration, *Meteorol. Atmos. Phys.*, 128, 39-56, doi:10.1007/s00703-015-0400-6, 2016.

651 Jin, X. P., Cai, X. H., Yu, M. Y., Song, Y., Wang, X. S., Kang, L. and Zhang, H. S.: Diagnostic analysis  
652 of wintertime PM2.5 pollution in the North China Plain: The impacts of regional transport and  
653 atmospheric boundary layer variation. *Atmos. Environ.*, 224, 117346, doi:  
654 10.1016/j.atmosenv.2020.117346, 2020.

655 Jin, X. P., Cai, X. H., Yu, M. Y., Wang, X. B., Song, Y., Wang, X. S., Zhang, H. S. and Zhu, T.: Regional  
656 PM2.5 pollution confined by atmospheric internal boundaries in the North China Plain: Analysis  
657 based on surface observations, *Sci. Total Environ.*, doi: 10.1016/j.scitotenv.2022.156728, 2022.

658 Jin, X. P., Cai, X. H., Yu, M. Y., Wang, X. S., Song, Y., Kang, L., Zhang, H. S. and Zhu, T.: Mesoscale  
659 structure of the atmospheric boundary layer and its impact on regional air pollution: A case study,  
660 *Atmos. Environ.*, 258, doi:10.1016/j.atmosenv.2021.118511, 2021.

661 Lareau, N.P., Crosman, E., Whiteman, C. D., Horel, J. D., Hoch, S.W., Brown, W.O.J. and Horst, T.W.:

662 The persistent cold-air pool study, *Bull. Amer. Meteor. Soc.*, 94, 51-63, doi: 10.1175/BAMS-D-11-

663 00255.1, 2013.

664 Li, J., Sun, J. L., Zhou, M. Y., Cheng, Z. G., Li, Q. C., Cao, X. Y. and Zhang, J. J.: Observational analyses

665 of dramatic developments of a severe air pollution event in the Beijing area. *Atmos. Chem. Phys.*

666 18, 3919-3935, doi: 10.5194/acp-18-3919-2018, 2018.

667 Li, Q. H., Wu, B. G., Liu, J. L., Zhang, H. S., Cai, X. H. and Song, Y.: Characteristics of the atmospheric

668 boundary layer and its relation with PM<sub>2.5</sub> during haze episodes in winter in the North China Plain.

669 *Atmos. Environ.* 223, 117265, doi: 10.1016/j.atmosenv.2020.117265, 2020.

670 Liu, N., Zhou, S., Liu, C. S., and Guo, J. P.: Synoptic circulation pattern and boundary layer structure

671 associated with PM<sub>2.5</sub> during wintertime haze pollution episodes in Shanghai, *Atmos. Res.*, 228,

672 186-195, doi:10.1016/j.atmosres.2019.06.001, 2019.

673 Liu, S. and Liang, X. Z.: Observed diurnal cycle climatology of planetary boundary layer height, *J.*

674 *Climate*, 23(21), 5790–5809, doi:10.1175/2010jcli3552.1, 2010.

675 Lu, R. and Turco, R. P.: Air pollution transport in a coastal environment II: 3-dimension simulations over

676 Los-Angeles basin, *Atmos. Environ.*, 29(13), 1499-1518, doi:10.1016/1352-2310(95)00015-q,

677 1995.

678 Lyu, W., Li, Y., Guan, D. B., Zhao, H. Y., Zhang, Q., and Liu, Z.: Driving forces of Chinese primary air

679 pollution emissions: an index decomposition analysis, *Journal of Cleaner Production*, 133, 136-144,

680 doi:10.1016/j.jclepro.2016.04.093,2016.

681 Mahrt, L.: Stratified atmospheric boundary layers and breakdown of models, *Theoretical and*

682 *Computational Fluid Dynamics*, 11, 263-279, doi:10.1007/s001620050093,1998.

683 Mayfield, J. A. and Fochesatto, G. J.: The Layered Structure of the Winter Atmospheric Boundary Layer

684 in the Interior of Alaska, *J. Appl. Meteorol. Climatol.*, 52, 953-973, doi:10.1175/jamc-d-12-01.1,

685 2013.

686 McNider, R. T. and Pour-Biazar, A.: Meteorological modeling relevant to mesoscale and regional air

687 quality applications: a review, *J. Air Waste Manage. Assoc.*, 70, 2-43,

688 doi:10.1080/10962247.2019.1694602, 2020.

689 Miao, Y. C. and Liu, S. H.: Linkages between aerosol pollution and planetary boundary layer structure

690 in China, *Sci. Total Environ.*, 650, 288-296, doi:10.1016/j.scitotenv.2018.09.032, 2019.

691 Miao, Y. C., Hu, X. M., Liu, S. H., Qian, T. T., Xue, M., Zheng, Y. J. and Wang, S.: Seasonal variation of

692 local atmospheric circulations and boundary layer structure in the Beijing-Tianjin-Hebei region and

693 implications for air quality, *J. Adv. Model. Earth Syst.*, 7(4), 1602-1626,

694 doi:10.1002/2015ms000522, 2015.

695 Narasimha, R., Sikka, D. R. and Prabhu, A.: The Monsoon Trough Boundary Layer. *Indian Academy of*

696 Sciences, 422 pp, 1997.

697 Peng, H. Q., Liu, D. Y., Zhou, B., Su, Y., Wu, J. M., Shen, H., Wei, J. S., and Cao, L.: Boundary-Layer  
698 Characteristics of Persistent Regional Haze Events and Heavy Haze Days in Eastern China, *Adv.*  
699 *Meteorol.*, doi:10.1155/2016/6950154, 2016.

700 **Petaja Petäjä**, T., Jarvi, L., Kerminen, V. M., Ding, A. J., Sun, J. N., Nie, W., Kujansuu, J., Virkkula, A.,  
701 Yang, X. Q., Fu, C. B., Zilitinkevich, S. and Kulmala, M: Enhanced air pollution via aerosol-  
702 boundary layer feedback in China. *Sci Rep* 6, 6, doi:10.1038/srep18998, 2016.

703 Pielke, R. A. and Uliasz, M.: Use of meteorological models as input to regional and mesoscale air quality  
704 models—Limitations and strengths. *Atmos. Environ.*, 32(8):1455–66, doi:10.1016/S1352-  
705 2310(97)00140-4, 1998.

706 Potty, K. V. J., Mohanty, U. C., and Raman, S.: Simulation of boundary layer structure over the Indian  
707 summer monsoon trough during the passage of a depression, *J. Appl. Meteorol.*, 40, 1241-1254,  
708 doi:10.1175/1520-0450(2001)040<1241:soblso>2.0.co;2, 2001.

709 Prezerakos, N. G.: Lower tropospheric structure and synoptic scale circulation patterns during prolonged  
710 temperature inversions over Athens, Greece, *Theor. Appl. Climatol.*, 60, 63-76,  
711 doi:10.1007/s007040050034, 1998.

712 Qu, K., Wang, X. S., Yan, Y., Shen, J., Xiao, T., Dong, H. B., Zeng, L. M. and Zhang, Y. H.: A comparative  
713 study to reveal the influence of typhoons on the transport, production and accumulation of O-3 in  
714 the Pearl River Delta, China, *Atmos. Chem. Phys.*, 21, 11593-11612, doi:10.5194/acp-21-11593-  
715 2021, 2021.

716 Rajkumar, G., Saraswat, R. S., and Chakravarty, B.: Thermodynamical structure of the monsoon  
717 boundary-layer under the influence of a large-scale depression, *Bound.-Layer Meteor.*, 68, 131-137,  
718 doi:10.1007/bf00712667, 1994.

719 Ren, Y., Zhang, H. S., Wei, W., Wu, B. G., Cai, X. H. and Song, Y.: Effects of turbulence structure and  
720 urbanization on the heavy haze pollution process, *Atmos. Chem. Phys.*, 19, 1041-1057,  
721 doi:10.5194/acp-19-1041-2019, 2019.

722 Rogers, R. E., Deng, A. J., Stauffer, D. R., Gaudet, B. J., Jia, Y. Q., Soong, S. T. and Tanrikulu, S.:  
723 Application of the Weather Research and Forecasting Model for Air Quality Modeling in the San  
724 Francisco Bay Area, *J. Appl. Meteorol. Climatol.*, 52, 1953-1973, doi:10.1175/jamc-d-12-  
725 0280.1,2013.

726 Sanders, F., and Doswell, C. A.: A case for detailed surface-analysis, *Bull. Amer. Meteorol. Soc.*, 76(4),  
727 505-521, doi:10.1175/1520-0477(1995)076<0505:acfdsa>2.0.co;2,1995.

728 Seaman, N. L. and Michelson, S. A.: Mesoscale meteorological structure of a high-ozone episode during  
729 the 1995 NARSTO-Northeast study, *J. Appl. Meteorol.*, 39, 384-398, doi:10.1175/1520-  
730 0450(2000)039<0384:mmsoah>2.0.co;2, 2000.

731 Seaman, N. L.: Meteorological modeling for air-quality assessments. *Atmos. Environ.* 34 (12–14):2231–  
732 59, doi:10.1016/S1352-2310(99)00466-5., 2000.

733 Seibert, R.: South foehn studies since the ALPEX experiment, *Meteorol. Atmos. Phys.*, 43, 91–103,  
734 doi:10.1007/BF01028112, 1990.

735 Sinclair, V. A., Belcher, S. E., and Gray, S. L.: Synoptic Controls on Boundary-Layer Characteristics,  
736 *Bound.-Layer Meteor.*, 134, 387-409, doi:10.1007/s10546-009-9455-6, 2010.

737 Sinclair, V. A.: A 6-yr Climatology of Fronts Affecting Helsinki, Finland, and Their Boundary Layer  
738 Structure, *J. Appl. Meteorol. Climatol.*, 52, 2106-2124, doi:10.1175/jamc-d-12-0318.1, 2013.

739 Stull, R.: *An Introduction to Boundary Layer Meteorology*. Springer, New York, 1988.

740 Talbot, C., Augustin, P., Leroy, C., Willart, V., Delbarre, H., and Khomenko, G.: Impact of a sea breeze  
741 on the boundary-layer dynamics and the atmospheric stratification in a coastal area of the North Sea,  
742 *Bound.-Layer Meteor.*, 125, 133-154, doi:10.1007/s10546-007-9185-6, 2007.

743 Tennekes, H.: The atmospheric boundary layer. *Phys. Today* 27, 52–63, doi:10.1063/1.3128397, 1974.

744 Travis, K. R., Jacob, D. J., Fisher, J. A., Kim, P. S., Marais, E. A., Zhu, L., Yu, K., Miller, C. C., Yantosca,  
745 R. M., Sulprizio, M. P., Thompson, A. M., Wennberg, P. O., Crounse, J. D., St Clair, J. M., Cohen,  
746 R. C., Laughner, J. L., Dibb, J. E., Hall, S. R., Ullmann, K., Wolfe, G. M., Pollack, I. B., Peischl, J.,  
747 Neuman, J. A., and Zhou, X. L.: Why do models overestimate surface ozone in the Southeast United  
748 States?, *Atmos. Chem. Phys.*, 16, 13561-13577, doi:10.5194/acp-16-13561-2016,2016.

749 Wang, W. G., Liu, M. Y., Wang, T. T., Song, Y., Zhou, L., Cao, J. J., Hu, J. N., Tang, G. G., Chen, Z., Li,  
750 Z. J., Xu, Z. Y., Peng, C., Lian, C. F., Chen, Y., Pan, Y. P., Zhang, Y. H., Sun, Y. L., Li, W. J., Zhu,  
751 T., Tian, H. Z., and Ge, M. F.: Sulfate formation is dominated by manganese-catalyzed oxidation of  
752 SO<sub>2</sub> on aerosol surfaces during haze events, *Nat. Commun.*, 12, doi:10.1038/s41467-021-22091-  
753 6,2021.

754 Xiao, Z. S., Miao, Y. C., Du, X. H., Tang, W., Yu, Y., Zhang, X., and Che, H. Z.: Impacts of regional  
755 transport and boundary layer structure on the PM<sub>2.5</sub> pollution in Wuhan, Central China, *Atmos.*  
756 *Environ.*, 230, doi:10.1016/j.atmosenv.2020.117508, 2020.

757 Ye, X. X., Song, Y., Cai, X. H., Zhang, H. S.: Study on the synoptic flow patterns and boundary layer  
758 process of the severe haze events over the North China Plain in January 2013, *Atmos. Environ.*  
759 *Times* 124, 129–145. doi:10.1016/j. atmosenv.2015.06.011, 2016.

760 Zhang, Q., Zheng, Y. X., Tong, D., Shao, M., Wang, S. X., Zhang, Y. H., Xu, X. D., Wang, J. N., He, H.,  
761 Liu, W. Q., Ding, Y. H., Lei, Y., Li, J. H., Wang, Z. F., Zhang, X. Y., Wang, Y. S., Cheng, J., Liu, Y.,  
762 Shi, Q. R., Yan, L., Geng, G. N., Hong, C. P., Li, M., Liu, F., Zheng, B., Cao, J. J., Ding, A. J., Gao,  
763 J., Fu, Q. Y., Huo, J. T., Liu, B. X., Liu, Z. R., Yang, F. M., He, K. B., and Hao, J. M.: Drivers of  
764 improved PM<sub>2.5</sub> air quality in China from 2013 to 2017, *Proc. Natl. Acad. Sci. U. S. A.*, 116, 24463-  
765 24469, doi:10.1073/pnas.1907956116, 2019.

766 Zhang, Q. Q., Ma, Q., Zhao, B., Liu, X. Y., Wang, Y. X., Jia, B. X., and Zhang, X. Y.: Winter haze over  
767 North China Plain from 2009 to 2016: Influence of emission and meteorology, *Environ. Pollut.*, 242,  
768 1308-1318, doi:10.1016/j.envpol.2018.08.019, 2018.

769 Zhao, C. Wang, F., Y., Shi, X. Q., Zhang, D. Z., Wang, C. Y., Jiang, J. H., Zhang, Q., and Fan, H.:  
770 Estimating the Contribution of Local Primary Emissions to Particulate Pollution Using High-  
771 Density Station Observations, *J. Geophys. Res.-Atmos.*, 124, 1648-1661,  
772 doi:10.1029/2018jd028888,2019.